JOURNAL OF MATERIALS SCIENCE 21 (1986) 2597–2622

Review
Tetrahedrally close-packed phases in superalloys: new phases and domain structures observed by high-resolution electron microscopy

K. H. KUO, H. Q. YE, D. X. LI
Laboratory of Atom Image of Solids, Institute of Metal Research, Academia Sinica, 110015 Shenyang, Peoples Republic of China

The structure of tetrahedrally close-packed phases (known also as Frank–Kasper phases) in superalloys has recently been extensively studied at the atomic level by high-resolution electron microscopy (HREM) in the Laboratory of Atom Image of Solids, Academia Sinica. In addition to a magnitude of domain structures, no less than six new phases have been found. This is a resumé of the study. First, a brief description of the crystal structures of these phases is given to illustrate the capability of HREM in revealing the building of complex structures from simple structural units. Secondly, the crystallographic features of the new phases and microdomain structures are discussed. Finally, the principle of juxtaposition of parallel oriented coordination polyhedra in these tetrahedrally close-packed phases is presented and this not only explains the existing structures of such phases but may also be important in the study of the quasi-crystalline state in rapidly quenched amorphous alloys.

1. Introduction

The term tetrahedrally close-packed phase (tcp) was coined to denote an intermetallic compound consisting mainly of tetrahedra in its crystal structure. This class of phases occurs frequently in transition metal systems and therefore also in many high alloy steels and superalloys. It is well known that the appearance of the σ, Laves or μ phase, being all tcp phases, in steels and superalloys will cause severe embrittlement and consequently the crystal structure, morphology and precipitation process of these tcp phases as well as their influences on the mechanical properties have been extensively studied in the past.

Bain and Griffith [1] discovered as early as 1927 that the embrittlement of Fe–Cr alloys and stainless steels was caused by the precipitation of a compound with the composition of FeCr. Thereafter many intermetallic phases with a similar crystal structure have been found in various binary and ternary systems of transition metals and they all are called the σ phase. At about the same time, Friauf [2] determined the crystal structures of $MgCu_2$ and $MgZn_2$. Somewhat later, Laves and Löhberg [3] determined the structure of $MgNi_2$ and at the same time they pointed out the close structural relationship between $MgCu_2$ (C15 type), $MgZn_2$ (C14 type) and $MgNi_2$ (C36 type). These tcp phases belong to the same structure family with an atomic size ratio of 1.2:1 and they are now called Laves or Friauf–Laves phase. The crystal structure of a closely related compound, the μ phase, was determined by Arnfelt and Westgren [4] in 1935. A great advance in the study of tcp phases took place in the fifties in conjunction with the rapid development of superalloys used in the jet engines. The structure of the σ phase was found to be isostructural to β-U [5]. Beck and his co-workers [6] discovered a series of new phases in many ternary systems of transition metals and their crystal structures were later determined by D. P. Shoemaker and C. B. Shoemaker, such as the P phase in Mo–Ni–Cr [7], R in Mo–Co–Cr [8], δ in Mo–Ni [9] and M in Nb–Ni–Al [10]. Although the phases Cr_3Si and Zr_4Al_3 have not been found in superalloys, they nevertheless are very important tcp phases because they are the elementary building blocks of other complex tcp phases. The structure of Cr_3Si was determined in 1931 [11], although that of Zr_4Al_3 was determined much later [12]. The crystallographic data of various tcp phases are presented in Table I.

Frank and Kasper [13, 14] made a systematic analysis of the characteristics of these tcp phases and their main conclusions were: first, there are only four coordination polyhedra with triangulated surface with a coordination number of 12, 14, 15 or 16 in these close-packed structures; secondy, these tcp phases are layer compounds made of primary and secondary layers. For instance, the σ structure can be considered as composed mainly of parallel oriented CN14 polyhedra with a primary layer consisting of hexagons and triangles at $z = 0$ and $\frac{1}{2}$ and a secondary layer of squares and triangles at $z = \frac{1}{4}$ and $\frac{3}{4}$ (Fig. 1). The atoms of the secondary layer are situated at the centres

0022–2461/86 $03.00 + .12 © *1986 Chapman and Hall Ltd.*

TABLE I Crystal structures of tetrahedrally close-packed phases

Phase	Example	Space group	Lattice constants (nm)			Atoms per cell
			a	*b*	*c*	
A15	Cr_3Si	*Pm3m*	0.4564			8
Zr_4Al_3	Zr_3Al_3	$P\bar{6}$	0.5433		0.5390	7
σ	$Cr_{46}F_{54}$	$P4_2/mnm$	0.8800		0.4544	30
C15	$MgCu_2$	*Fd3m*	0.7080			24
C14	$MgZn_2$	$P6_3/mmc$	0.516		0.850	12
C36	$MgNi_2$	$P6_3/mmc$	0.527		1.33	24
μ	Mo_6Co_7	$R\bar{3}m$	0.4762		2.5615	39
M	$Nb_{48}Ni_{38}Al_{13}$	*Pnam*	0.9303	1.6266	0.4933	52
P	$Mo_{42}Cr_{18}Ni_{40}$	*Pbnm*	0.9070	1.6983	0.4752	56
δ	MoNi	$P2_12_12_1$	0.9108	0.9108	0.8852	56
R	$Mo_{31}Cr_{18}Co_{51}$	$R\bar{3}$	1.0903		1.9342	159

(and two vertices) of these CN14 polyhedra and therefore the network of the secondary layer can be used as a representation of the tessellation of these parallel-oriented polyhedra. Using the Schläfli notation where numbers representing polygons are arranged according to the order of their appearance surrounding a node of this network, the secondary layer or the characteristics of the σ structure is 3 3 4 3 4 or 3^2434. Based upon this kind of analysis, Frank and Kasper postulated the possibility of the existence of two σ-related structures with a secondary network of 3^342 or $3^6 + 3^2434$ (1 : 6). Frank and Kasper also pointed out that the structures of the Laves and μ phases consist mainly of icosahedra (CN12) with the primary layer of pentagons and triangles perpendicular to the *3* or *6* axis. Somewhat later, Shoemaker and Shoemaker [15] classified these tcp structures according to the main polygons in the primary layer into three categories: 1, hexagons; 2, pentagons; 3, a mixture of pentagons and hexagons.

Recently Andersson [16] pointed out that complex close-packed structures can be visualized as made of some simple elementary structural units by crystallographic symmetry operations such as rotation,

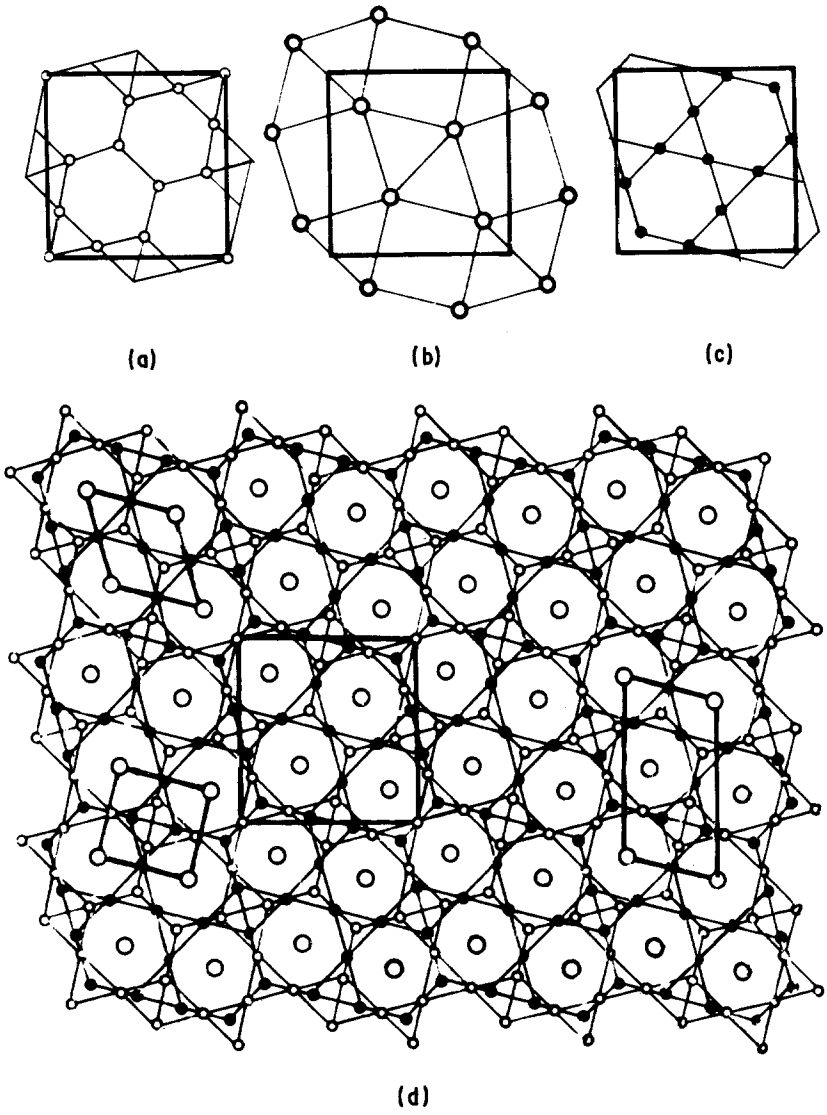

Figure 1 Schematic diagram of the layer structure of σ. (a) $z = 0$; (b) $z = \frac{1}{4}$ and $\frac{3}{4}(3^2434)$; (c) $z = \frac{1}{2}$, and (d) projected on (0 0 1), unitcells of Cr_3Si (small square), Zr_4Al_3 (rhombus) and σ (large square) are outlined.

reflection, inversion and a combination of these. This greatly simplifies the analysis of the structural relationships between these tcp phases as well as the structural defects in them, such as domain boundaries.

The structural defects in these tcp structures have been studied only sporadically [17–19] until recently. Thanks to the recent development of high-resolution electron microscopy (HREM) to a level of atomic resolution, defects in these structures have become the subject of study in the last five years in many HREM laboratories [20–29]. For instance, the stacking faults in the σ phase [23, 24], long-period ordered structures in Laves phases [25], planar faults in χ [26], μ [27], M [28] and P [29] phases. This adds greatly to our knowledge of the planar faults in complicated tcp structures.

However, these investigation were made on samples of intermetallic phases specially melted from pure metals with rather simple compositions at the equilibrium state. This will differ from the tcp phases precipitated in superalloys with fairly complex compositions. Therefore, we have devoted ourselves in the past three years to a study of the tcp phases in industrial superalloys by HREM and selected-area electron diffraction (SAD) and we are fortunate in discovering no less than six new tcp phases and a magnitude of microdomain structures. This review is a resumé of our recent publications. First, a brief description of the crystal structures of these tcp phases is given to illustrate the capability of HREM in revealing the building of complex structures from simple structural units. Secondly, we shall discuss the crystallographic features of these new tcp phases and microdomain structures found by us. Finally, the principle of juxtaposition of parallel-oriented coordination polyhedra in these tcp phases will be presented and this will not only explain the existing structures of these tcp phases but may also be important in the study of quasi-crystalline state in rapidly quenched amorphous alloys.

2. Description of tcp structures

The structures of tcp phases will be analysed successively, though only briefly, in the light of coordination polyhedra, layer networks as well as hexagonal and pentagonal antiprisms.

2.1. Coordination polyhedra

A coordination polyhedron is that formed by connecting all nearest neighbour atoms surrounding an atom at the centre; the coordination number, CN, is the number of these nearest neighbouring atoms. In pure metals where the atoms are of equal size, the highest CN is 12 as in the case of fcc and hcp structures. However, in the case of alloys or intermetallic compounds where atoms of different sizes exist, the highest CN can be 12, 14, 15 or 16 according to the sizes of two atoms species [30]. First an icosahedron with CN 12 will be discussed, see Fig. 2a. The atoms at the 12 vertices of this icosahedron form 20 equilateral triangles. The distance from the centre atom to these 12 atoms are all equal but they are about 5% shorter than than the distance between atoms at the vertices or the coordination shell. In other words, the atom located at the centre is about 20% smaller than those at the vertices (recall the Laves phases having an atomic size ratio of 1.2 : 1). This icosahedron consists of 20 tetrahedra, though obviously not regular, and no octahedra; therefore it has a higher packing density than the close-packed structures with the same CN12 of pure metals. There are six five-fold axes in this icosahedron and it is impossible to fill a space completely with these icosahedra. However, it has been pointed out by Kasper [30] that penetrating the tetrahedral polyhedra of different CN with these icosahedra will make the filling so perfect that no empty space exists. It should be pointed out that in the cases of CN14, 15 and 16 polyhedra the triangles of the triangulated surface, unlike those in the CN12 icosahedra, are somewhat distorted and the size of the atom at the centre increases with the coordination number.

The CN12 icosahedron can be visualized as two pentagonal prisms placed one over the other antisymmetrically (Fig. 2a) having a point group symmetry $\bar{5}\bar{3}m$ (Fig. 2c). Fig. 2b represents a projection along one of the five-fold axes showing a dense population of atoms on the periphery consisting of two pentagons and a slightly populated interior. This pentagonal "tunnel" can be imaged in a high-resolution electron microscope as a white or bright dot.

The CN14 polyhedron consists of 24 tetrahedra forming a hexagonal antiprism with 24 triangles on the surface having a point group symmetry $\overline{12}2m$ (Fig. 3). Fig. 3b is a projection along this $\overline{12}$ axis and the hexagonal antiprism now appears, like the pentagonal tunnel in Fig. 2b, as a hexagonal tunnel.

The CN15 polyhedron looks like a triangular column with hexagonal prisms on its three columnar surfaces (Fig. 4) having point group symmetry $\bar{6}m2$. Since it exists in the structure ofthe rhombohedral μ phase it is sometimes called the μ polyhedron. There are altogether 26 tetrahedra in this CN15 polyhedron with 26 triangles on the surface.

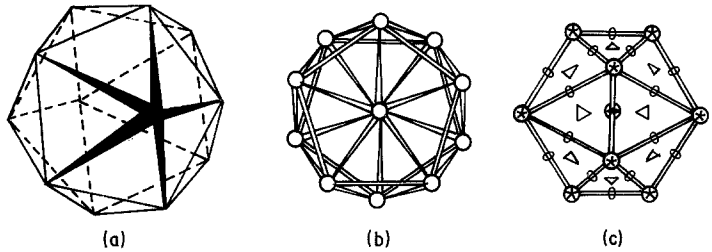

Figure 2 (a) CN12 icosahedron; (b) projection along the five-fold axis and (c) icosahedral symmetry $\bar{5}\bar{3}m$.

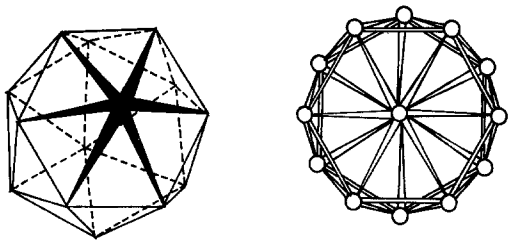

Figure 3 (a) CN14 polyhedron and (b) projection along the hexagonal axis.

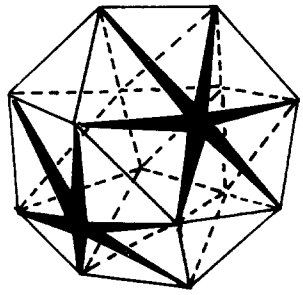

Figure 5 CN16 polyhedron.

The CN16 polyhedron has the highest coordination number and it looks like large truncated tetrahedron with four hexagonal prisms on its tetrahedral surface (Fig. 5) with a point group symmetry of $\bar{4}\bar{3}m$. Since it occurs frequently in the Laves of Friauf–Laves phase, it is commonly called the Friauf–Laves polyhedron.

Coordination polyhedra are used to describe the nearest neighbour relationship of the tcp structures. In real crystal structures different coordination polyhedra are entangled together forming a penetrating complex so that the atom at the centre of one polyhedron may be situated at the periphery of another or *vice versa*. Furthermore, in order to fill space completely, or conform to the lattice translation, these polyhedra may be subjected to slight deformation when they are put together. However, the principle of filling a space with differently oriented tetrahedra remains true.

The occupancy of atoms on these different CN sites depends upon the atomic sizes.The transition metals to the right of manganese in the Periodic Table together with aluminium and silicon usually occupy the CN12 sites while to the left of manganese are those with a somewhat larger atomic radius, the CN15 and CN16 sites. The occupancy of the CN14 sites is mixed, or by the metals to the right of manganese. Manganese may take either of these sites depending upon with which metal it forms an intermetallic compound.

2.2 Atomic layers

One of the characteristics of the tcp structures is the fact that most of them also belong to layer structures. Among the 11 tcp structures listed in Table I, only R and δ structures are deviated, though only locally, from a layer structure. This simplifies greatly the analysis of the crystal structures of the tcp phases once the primary and secondary layers in them can be discerned. In Section 1 it has already been pointed out in connection with the σ structure that the atoms in the secondary layer represent the centre position of the CN14 polyhedra and the atoms on the primary layer (the hexagons) the nature of the polyhedra (CN14 hexagonal antiprisms).

In the case of the μ phase consisting mainly of icosahedra (Fig. 6), the primary layer in the [1 1 0] projection is a network of triangles and pentagons ($3\,5^3 + 3\,5\,3\,5 + 3^2\,5^2 + 3\,5\,3^2\,5$) with the later being in antisymmetrical positions. The atoms in the centres of the CN12 icosahedra are arranged in A″AB″BC″C . . . layer sequence, where A, B and C are the notation used to denote the sites in fcc packing, though here they represent compound layers as shown in Fig. 6 Compound layers A and A″ have a similar, but different, arrangement of layers, so have B and B″, as well as C and C″. This kind of analysis can also apply to other tcp phases with a *3* or *6* axis, for instance, the Laves phase, etc. (Fig. 7). The advantage of using this kind of notation is its wide use in the literture in the study of crystalline defects such as stacking faults and dislocation, as well as twins and long-period ordered structures. However, the readers have to keep in mind that here we are dealing with compound layers of icosahedra instead of simple atomic layers [31, 32].

The advantage of the layer description of crystal structures is its two-dimensional nature which is much easier to comprehend than the space distribution of coordination polyhedra. However, they do not contradict each other and the layer description is just another mainfestation of the tessellation of the coordination polyhedra as the latter are projected along a certain direction. Fig. 8 shows the different tesselations of these coordination polyhedra in which the different CN sites are illustrated with circles of different sizes. To the right are the characteristic secondary layers of various structural units, which will be discussed further in the following section.

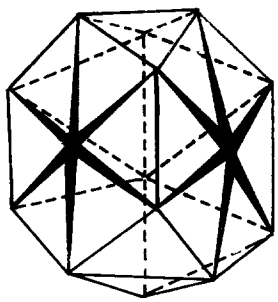

Figure 4 CN15 polyhedron.

2.3. Structural units

As mentioned above, there are only four different kinds of coordination polyhedra in tcp structures and in the case of CN12 and CN14 polyhedra the pentagonal and hexagonal antiprisms are juxtaposed in parallel orientation. Shoemaker and Shoemaker [15] and Andersson [16] considered some simple units composed of these antiprisms such as parallelograms and rectangles as elementary structural units in the tcp structures. Since these antiprisms can be

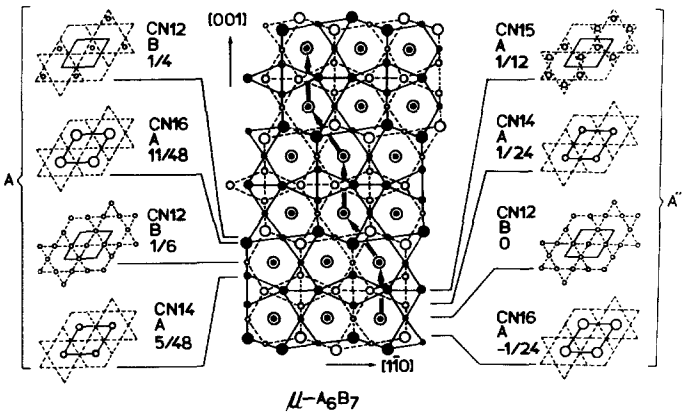

Figure 6 Schematic drawing of the layer structure of projected on (1 1 0) consisting alternately of Zr_4Al_3 and $MgCu_2$ units in [0 0 1] direction. Compound layers A and A″ are also shown.

pentagonal, hexagonal or a mixture of these, there are altogether six different structural units as shown in Fig. 8. In the case of hexagonal antiprisms, all the CN14 polyhedra are face-sharing and therefore have the same separation between them. This makes the Zr_4Al_3 structure unit a rhombus and Cr_3Si a square. However, in the case of pentagonal antiprisms, the CN12 icosahedra are either face- or edge-sharing thus having different separations. The triangles in the $MgCu_2$ unit are isosceles and the angle facing the long side is 72° and the other two 54°. The Zr_4Al_3 unit in (1 0 0) projection becomes a rectangle with the ratio of long : short sides quite close to that of the $MgCu_2$ unit. This will have an important bearing in the formation of domain structures of the pentagonal tcp phases (see Section 5.2).

2.4. Classification of tcp phases

2.4.1. Hexagonal antiprisms – σ-phase related structures

The elementary structural units of this class of tcp phases are Cr_3Si with a 4^4 network and Zr_4Al_3 a 3^6 one, and in Fig. 9 they are classified as the first-order structures. The structure of σ-phase consists of these two kinds of units arranged in the 3^2434 scheme. Another combination of these units is 3^34^2 and this is the structure of the newly discovered H phases [33, 34]. They are considered as second-order structures of this class of tcp phases (for details, see Figs. 19 and 21). Following this principle, third-order structures can be built from the second-order ones; for instance, the newly found J phase has a network of $3^6 + 3^34^2$ and both the F and K phases consist of the same $3^6 + 3^2434$ units but in different proportions. These complex structures were discovered only recently by means of HREM [35] and they are shown on the right of Fig. 9. More details can be found in Figs. 25, 27 and 30.

2.4.2. Pentagonal antiprisms – Laves phase-related structures

The elementary structural units of this class of tcp phases are the $MgCu_2$ parallelogram and Zr_4Al_3 rectangle [projected on (1 1 0)]. Neighbouring antiprisms have two different separations: a shorter one, *s*, for face-sharing icosahedra and a longer one, *l*, for edge-sharing ones (see Figs. 46 and 48). Only the centres of these pentagonal antiprisms are drawn in Fig. 10 and these two first-order structures are shown on the left. Since they both have nearly the same *l* and *s*, an $MgCu_2$ unit can attach to a Zr_4Al_3 unit by sharing either the *l* or the *s* side. This renders it possible to form many varieties of complex second and third-order structures as illustrated in Fig. 10. The

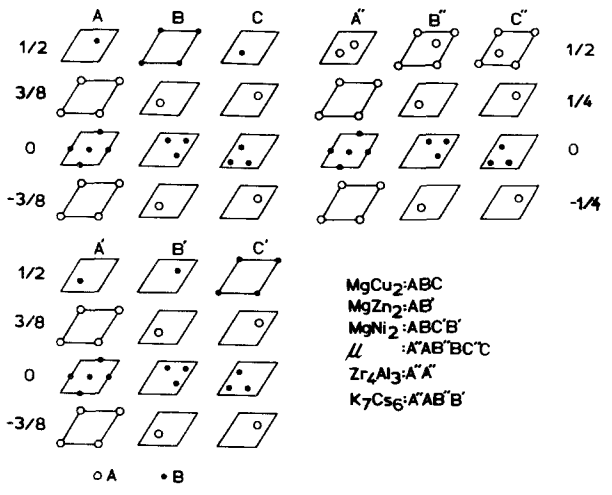

Figure 7 Stacking of compound layers in various pentagonal tcp phases.

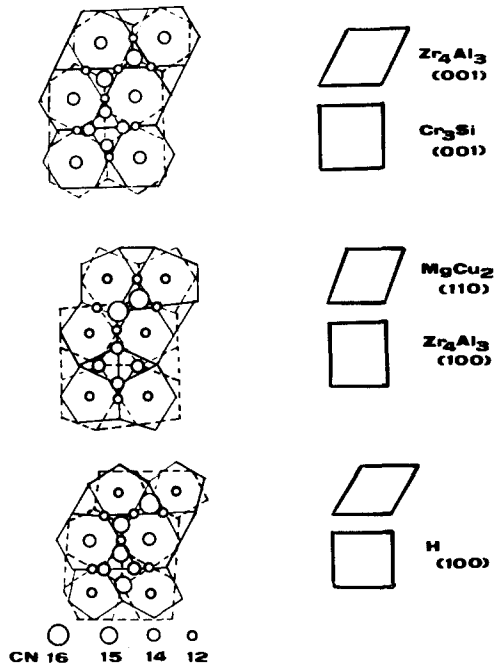

Figure 8 Six possible configurations of antiprisms (left) and elementary structure units (right) in tcp phases.

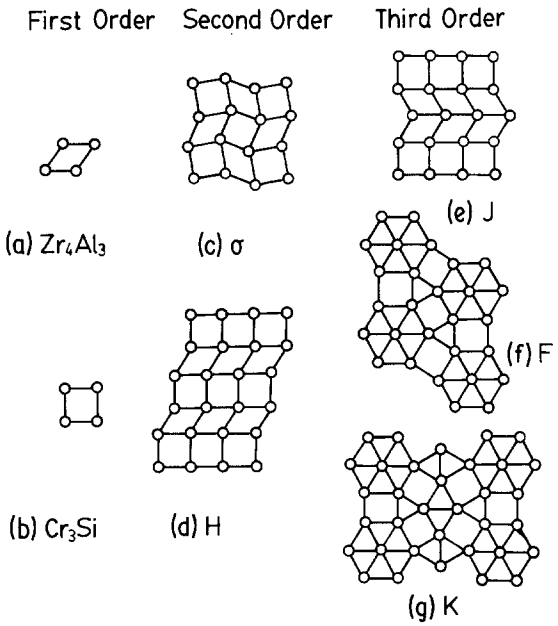

Figure 9 Classification of hexagonal tcp phases. Higher order structures are built up with lower order structure units.

secondary layer of the $MgCu_2$ unit is a distorted 3^6 network and if 3 and *3* are used to differentiate the triangles with 54° and 72°, respectively, at the apex, then the $MgCu_2$ layer should have a $(3^2 3)_2$ network. A succession of $MgCu_2$ units forms the C15 ($MgCu_2$ type) Laves phase and the $MgCu_2$ units in twin positions the C14 ($MgZn_2$ type) and C36 ($MgNi_2$ type) Laves phases. Alternate layers of $MgCu_2$ and Zr_4Al_3 results in the structures of the μ and K_7Cs_6 phases. All these are classified as second-order structures consisting of pentagonal antiprisms. A slab of C14 Laves phase and another slab of μ phase will form a compound slab of the newly found C phase [36] which is isomorphous with the structure of C-silicide [37, 38]. Differently oriented μ slabs constitute a new type (W_2FeSi) of structure [39] which is sometimes called the "pentagonal σ-phase" [14, 40]. If these two differently oriented single μ slabs of this pentagonal σ-phase are substituted by double slabs, another third-order structure of the M phase will result [10].

2.4.3. Hexagonal–pentagonal antiprisms

The structure of the P phase has mixed hexagonal and pentagonal antiprisms and those of the R and δ phases may also belong to this class of tcp phases. Although there are some changes in the orientation of the antiprisms, the characteristics of this type of structure are still not very well understood and this offers opportunities for further investigations.

3. High-resolution electron microscopy

3.1. Specimen preparation

The composition and heat treatment of the alloys used are given in Table II. The precipitates of various phases were separated electrolytically from these alloys and ground in an agate mortar. They were then collected on holey carbon films for electron microscopic examination. Some thin slices cut from the alloys have also been used. They were first ground and then thinned down electrolytically by the double jet technique.

A JEM 200CX electron microscope equipped with a set of ultrahigh resolution pole pieces, capable of giving an interpretable resolution of 0.25 nm, was used [41]. Image simulation was done using the multi-slice programme written by Ishizuka [42].

3.2. Imaging conditions

In the past, X-ray diffraction has been the main technique for crystal structure determination. Although it can provide rather accurate atomic positions, there are nevertheless the average results of billions of unit cells. The resolution of electron microscopes has improved to such an extent in the last decade that atomic imaging becomes possible and the projection of a crystal structure in the direction of electron beam can be directly seen. Moreover, what it gives is the atomic configuration of local defects, microdomain or grain boundary, surfaces, etc. Therefore, HREM has been extensively used lately in research not only in solid state physics, chemistry, electronics, materials science and minerology [43–46], but also in molecular biology where the structures of virus and protein have been attacked with great success [47].

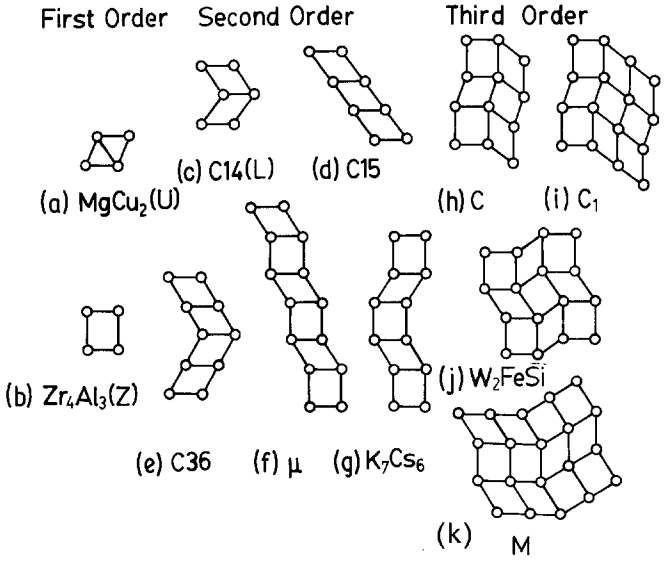

Figure 10 Classification of pentagonal tcp phases. Higher order structures are built up with lower order structure units.

TABLE II Chemical composition, heat treatment and related precipitates of superalloys tested

Composition								Heat Treatment		Precipitates
Cr	Ni	W	Mo	Al	Ti	Fe	Co	Temp. (° C)	Time (h)	
15.0	34.0	2.12	2.01	2.35	2.35	base	–	1140/700	2000	σ, H, Laves, C
8.7	base	–	3.05	6.25	5.68	0.35	10.2	850	200	σ, H
20.0	base	8.0	8.0	0.6	0.6	2.0	–	1050	2	σ, μ, F, K, J
15.0	40.0	4.0	2.0	2.0	2.6	base	–	1140/850	200	Laves, μ
13.0	42.5	–	6.0	0.35	2.35	base	–	900	3000	Laves, μ

When electrons pass through a crystal, they will bring with them the structural information of this crystal entering the imaging system of the electron microscope (Fig. 11). The transmission function $q(x, y)$ of the object will be transformed into a set of diffraction spectra $Q(h, k)$ at the back focal plane of the objective lens. These spectra will serve as secondary sources for interference and an image $q(x_i, y_i)$ can thus be reconstructed at the image plane. In order to obtain an interpretable high-resolution image, both the specimen and electron microscope have to satisfy a number of rigorous conditions. The specimen has to be very thin, usually less than 10 nm, so that when passing through the specimen the electron wave suffers only phase changes without any modification in amplitude, and it is therefore called a phase object. The transmission function of a phase object is $q(x, y) = \exp[i\sigma\phi(x, y)]$, where σ is the interaction constant and $\phi(x, y)$ the projected crystal potential in the beam direction depending upon distribution of atoms in the crystal. The electron microscope should be able to give a relatively perfect image from this transmission function. An ideal case is when all diffracted waves will take part in the imaging process and they should maintain a correct phase relationship. However, in reality only a limited number of diffracted beams can pass through the objective aperture at the back focal plane and the objective aperture function $P(h, k)$ is instituted to take this into account. $P(h, k) = 1$ for the beams falling inside of this aperture, otherwise, 0. Furthermore, in addition to the phase changes of the diffracted waves caused by the spherical aberration of the objective lens, the divergence of the source and chromatic aberration will degrade the image quality. Therefore, the transfer function of the objective is

$$A(h\,k) = P(h, k)\exp[2\pi i\chi(h, k)]B(h, k)C(h, k) \quad (1)$$

where

$$\chi(h, k) = [\Delta f\lambda(h^2 + k^2)/2 + C_s\lambda^3(h^2 + k^2)^2]/4$$

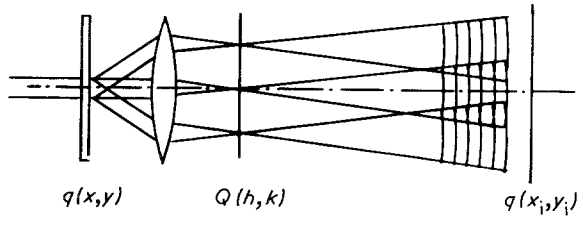

Figure 11 Imaging process of the objective lens in an electron microscope.

is the phase change caused by the spherical aberration coefficient, C_s, and the defocus, Δf, of the objective; $B(h, k)$ is the envelope function caused by the divergency of the source; and $C(h, k)$ is the envelope function caused by chromatic aberration.

For an ideal weak phase object, i.e. a thin crystal composed of light elements with low atomic numbers, the transmission function can be expanded as

$$q(x, y) = 1 + i\sigma\phi(x, y)$$

and it transforms into $Q(h, k)$ at the back focal plane

$$Q(h, k) = [\delta(h, k) + i\sigma\phi(h, k)]A(h, k)$$

The intensity distribution at the image is the conjugate product of the Fourier transform, $\mathcal{F}$, of the above function and after neglecting the second-order terms of $\sigma\phi$ this becomes

$$I(x_i, y_i) = 1 - 2\sigma\phi(x, y)^*\mathcal{F}[\sin\chi(h, k) \times P(h, k)B(h, k)C(h, k)] \quad (2)$$

If we neglect for the time being the effect of objective aperture, divergence of source and chromatic aberration, when $\sin\chi = -1$ the image contrast

$$I(x_i, y_i) - 1 = 2\sigma\phi(x, y)$$

is proportional to the projected crystal potential and is therefore called the structural image.

However, it is rather difficult to meet the rigorous requirements of the weak phase object. This is especially so where the t c p phase is concerned because it generally contains such heavy atoms as molybdenum and tungsten. In this case, $\sigma\phi(x, y)$ becomes greater than unity when the crystal thickness exceeds 2 to 3 nm; i.e. it is no longer a weak phase object. In fact, the crystallites under examination are usually thicker than 5 nm. Furthermore, it is also not possible to have all diffracted waves satisfying $\sin\chi = -1$ simultaneously. The term $\sin\chi$ contains three parameters, namely λ, C_s and Δf, and only the last can be adjusted to give as a broad region with approximate $\sin\chi = -1$ as possible (see Fig. 12). This Δf is generally called the optimum defocus and under this circumstance the value $\boldsymbol{k}$ where the transfer function curve intersects the abscissa represents the longest wave vector of the diffracted waves having the correct phase relationship, or the resolution limit, where a one to one correspondence exists between the image and the projected structure. Fig. 12 shows the transfer function curve of a JEM 200CX microscope equipped with ultrahigh-resolution pole pieces with a C_s = 1.2 mm working at a $\Delta f = -67$ nm and a point resolution of 0.25 nm.

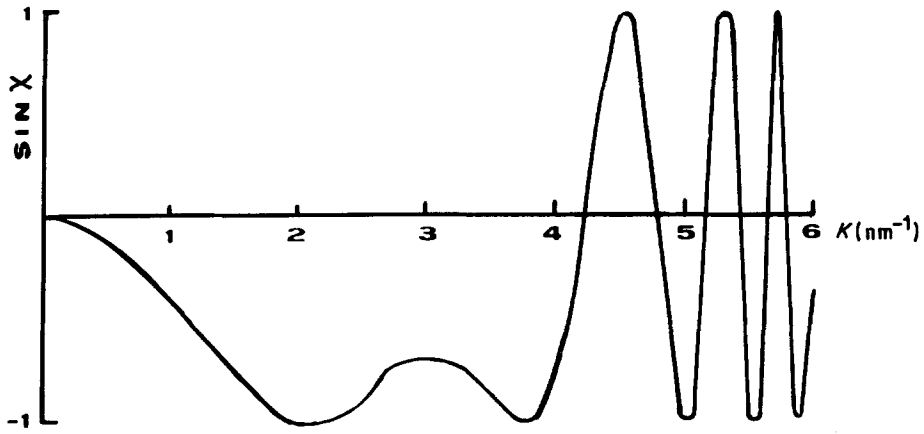

Figure 12 Phase-object transfer function of a JEM 200CX electron microscope at the optimum defocus (−67 nm) giving an interpretable resolution of about 0.25 nm (intersecting k at about 4 nm^{-1}).

Since the high-resolution image is only interpretable with respect to the projected structure under certain specimen conditions, it is necessary to compare it with the simulated image based on the structure model. In the following, the high-resolution images of the σ and μ phases will be used to illustrate the imaging conditions of tcp phases [34, 35].

Looking in the $[0\,0\,1]_\sigma$ direction (see Fig. 1d), the projected distances of the atoms located at the periphery of a hexagonal antiprism vary from 0.066 to 0.227 nm, much smaller than the resolution limit of a modern electron microscope. On the other hand, the separation of neighbouring antiprisms arranged in a 3^2434 scheme is 0.454 nm and this is much larger than the resolution limit of 0.25 nm. Moreover, the atom population inside the hexagonal antiprisms is so low that it behaves rather like hexagonal tunnels in the imaging process. Therefore it is possible to use the high-resolution image to show the tessellation of these hexagonal antiprisms in the σ structure. The central part of Fig. 13 is the structural image of σ in which the bright dots or discs show a 3^2434 network and there is a one to one correspondence between these bright dots in the image and the hexagonal tunnels in the projected structure model on the left. Moreover, the match between the simulated image on the right ($\Delta f = -67$ nm, $t = 5$ nm) and the high-resolution image is also very good. From such a comparison it can be concluded that in dealing with this kind of tcp structure with hexagonal antiprisms, the bright dots in the structural image taken at the optimum defocus condition can possibly represent the arrangement of these antiprisms. By this method the structures of the newly discovered H, F, K and J phases are directly "read" from their respective high-resolution structural images [33, 35].

A similar situation has been found in the case of tcp phases consisting of pentagonal antiprisms such as the μ phase illustrated in Fig. 14. Each bright dot in the structural image now represents a pentagonal antiprism (in Section 3.3 concerning electron diffraction, the problem of differenting these two kinds of antiprisms, pentagonal and hexagonal, will be discussed). The simulated image at $t = 5$ nm and the optimum defocus ($\Delta f = -67$ nm) shows an identical distribution of bright dots.

In a study of domain boundary structures, as in Fig. 15 (on the left), a supercell consisting of both domains as well as the boundary has to be chosen in order to obtain the simulated image (bottom right). Fig. 15 shows two parallel or translation domains of the C14 Laves phase and the match between the simulated ($\Delta f = -67$ nm, $t = 5$ nm) and observed images is also good and both are in agreement with the projected structure model. This proves that even complex domain structures can equally well be studied by means of HREM. As will be discussed further in Section 5, in the case of tcp phases the domain boundary structure in general is another tcp phase of the same class. In the above example the domain boundary structure in Fig. 15 is nothing else but a slab of the μ phase consisting also of pentagonal antiprisms as the C14 Laves phase. This explains why the domain boundary can be imaged just as the domains on both sides of it.

Fig. 15 also shows the capability of HREM in revealing local structures such as a domain boundary

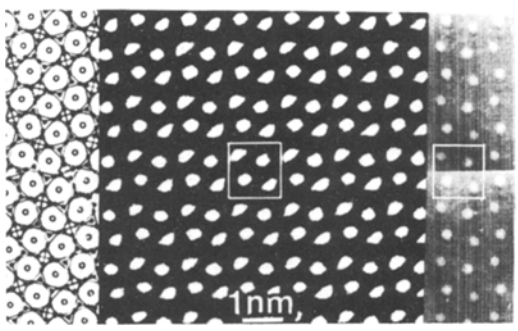

Figure 13 [0 0 1] structure model (left), high-resolution (middle) and simulated (right, $t = 5$ nm and $\Delta f = -67$ nm) images of σ.

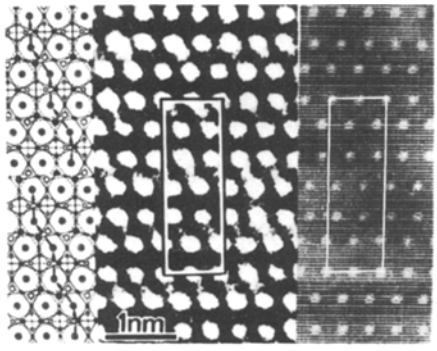

Figure 14 [0 0 1] structure model (left), high-resolution (middle) and simulated (right, $t = 5$ nm and $\Delta f = -67$ nm) images of μ.

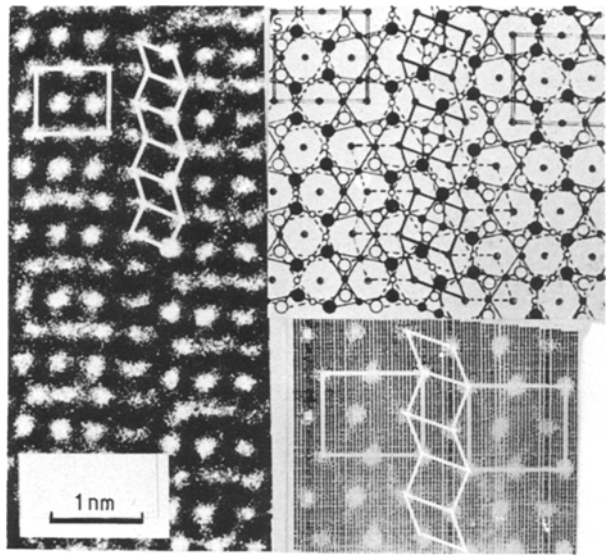

Figure 15 Structure model of the $(1\bar{1}0)$ domain boundary of the C14 Laves phase (top right) and its high-resolution image (left) and simulated image (right, $t = 5$ nm and $\Delta f = -67$ nm).

which is, in general, very difficult to detect by ordinary X-ray and electron diffraction methods. As will be illustrated in Section 5, a great number of domain boundary structures have thus been discovered recently by this technique.

The resolving power of the electron microscope is still in the process of continuing improvement. The new microscopes working at 300 or 400 kV have already attained a point resolution of 0.2 nm or even better, and this makes the imaging of single atoms realizable in many laboratories with commercial instruments. Even with a microscope of a point resolution of 0.25 nm, atoms with a separation of 0.22 nm can still be imaged as shown in Fig. 16, by defocusing further than the optimum value to move the intersection of the transfer function curve to a higher value of $\boldsymbol{k}$ at the sacrifice of resolution at other $\boldsymbol{k}$ values (the flat region of $\sin\chi = -1$ in Fig. 12 will move to the right but becomes much narrower). Fig. 16a is the atom image of Ni_3V in [1 1 0] orientation in which each bright dot represents a column of mixed nickel and vanadium atoms. The horizontal row of bright dots is the projection of the close-packed (1 1 1) plane and its stacking follows the ABC. . . sequence. On partial substitution of titanium for vanadium in this compound, a 9R polytype with the stacking sequence ABCBCACAB is formed, as can be seen directly from the atom image in Fig. 16b [46]. One would expect a new kingdom of microstructures to be revealed at the atom level in the near future by means of HREM.

3.3. Selected-area and convergent beam electron diffraction

From Section 3.2 it is clear that a bright dot in the high-resolution image can represent either a hexagonal or a pentagonal antiprism. In other words, such an image can show the translation symmetry of these antiprisms but not their point group symmetry. This is because at the present resolution of the electron microscope what have been imaged are the tunnels inside these antiprisms but not their fine structures. However, the electron diffraction pattern (EDP) reveals not only the translation symmetry of a phase but also its point group symmetry. Figs, 17a and b are, respectively, the [0 0 1] EDP of σ and the [1 1 0] EDP of μ. Besides the translation symmetry of the space lattice, which can be derived from these cross-grid patterns, the $\overline{12}$ and $\bar{5}$ symmetries of the hexagonal and pentagonal antiprisms are manifested by the 12 or 10 diffraction spots on the outermost rings in Figs. 17a and b respectively (marked with arrows). This will be further discussed in Section 6.

The convergent beam electron diffraction (CBED), because of its larger angle of incidence, can provide three-dimensional structure information of a crystalline phase such as the space lattice, point group as well as space group symmetries [48]. Recently, Lin and Steeds [49] determined the same space group of the F phase by means of CBED, at the same time as did Li and Kuo [35] using the HREM technique.

Fig. 18a is the [0 0 0 1] CBED pattern of the F phase with a *6mm* symmetry, the possible diffraction group being *6mm* or $6mm1_R$ and the corresponding point group symmetry being *6mm* or *6/mmm*. Similarly, Fig. 18b is the $[1\,0\,\bar{1}\,0]$ CBED pattern with a *2mm* symmetry, the possible diffraction group being *2mm* or $2mm1_R$ and the corresponding point group being $\bar{6}m2$ or *6/mmm*. From these two CBED patterns, the point group of F can be ascertained to be *6/mmm* [50].

Obviously, HREM shows directly the configuration of the antiprisms while CBED gives information concerning the point group symmetry of these antiprisms. A combination of these two techniques can characterize completely the structure of a crystalline phase which would be difficult using either method by itself.

4. New tetrahedrally close-packed phases

4.1. σ-phase related new phases: H, F, K and J

In their classical works on tcp structures, Frank and Kasper [13, 14] predicted, in 1959, hypothetical structures with 3^34^2 and $3^6 + 3^24341(1:6)$ tessellation of

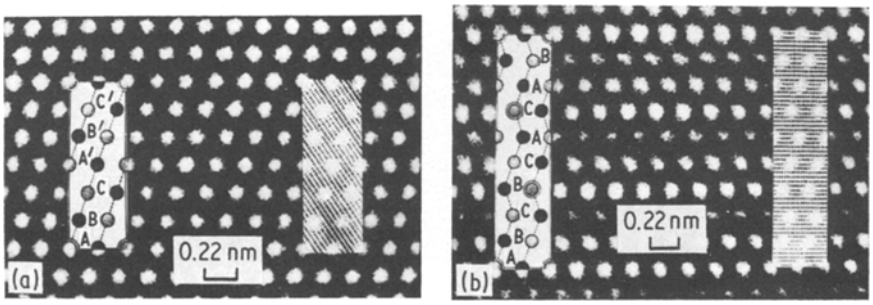

Figure 16 (a) [1 1 0] Atomic image of Ni_3V with insets of the structure model (left) and simulated image (right). (b) Same as (a) for the $Ni_3(V, Ti)$ 9R polytype.

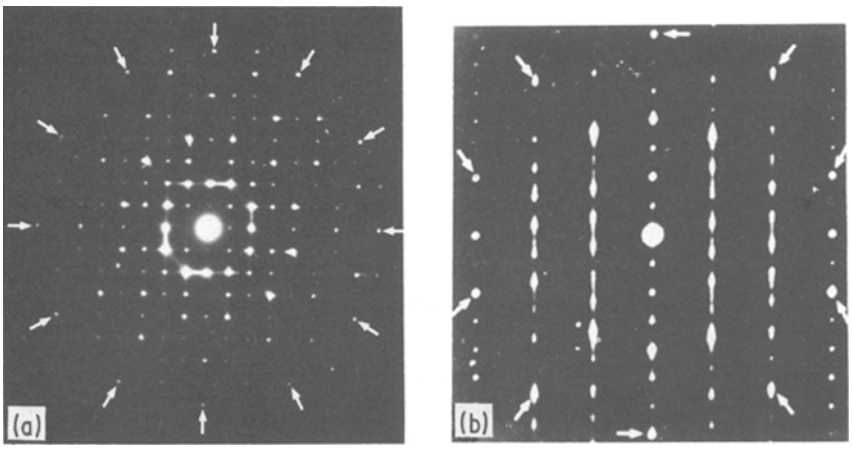

Figure 17 (a) [0 0 1] EDP of σ in which the 12 evenly distributed spots, marked with arrows, on the outermost ring imply the antiprisms being hexagonal. (b) [1 1 0] EDP of μ in which the 10 evenly distributed spots, marked with arrows, on the outermost ring imply the antiprisms being pentagonal.

hexagonal antiprisms. However, the experimental verification of their existence has been delayed until recently when we took up this problem with HREM [33, 35]. In the meantime, two more t c p phases with $3^6 + 3^2434(1:10)$ and $3^6 + 3^342(1:2)$ tessellations have also been found (see Table IX). In order to stress the importance of hexagonal antiprism in this class of t c p structures and to honour the great contribution of Frank and Kasper, three of these new phases are called H, F and K, respectively. The existence of F phase has also been found independently by Lin and Steeds mainly by CBED [49].

4.1.1. H phase [33, 34, 35]

The H phase with a 3^342 tessellation of hexagonal antiprisms has been found to intergrow frequently with the σ phase with a 3^2434 tessellation (Fig. 19). The σ phase has a tetragonal lattice while the H phase an orthorhombic one, and they are outlined in Fig. 19. They are composed of the same number of square Cr_3Si and triangular Zr_4Al_3 units and the only difference is their arrangement. Therefore, these two unit cells contain the same number of atoms and have the same unit cell volume.

From the juxtaposition of these two unit cells, the following crystallographic relationship can be found:

$$[1\,0\,0]_H \| [4\,\bar{1}\,0]_\sigma, \quad a_H = a_\sigma/(2\cos 14.03°) = 0.45\,\text{nm}$$
$$[0\,1\,0]_H \| [1\,4\,0]_\sigma, \quad b_H = 2a_\sigma \cos 14.03° = 1.75\,\text{nm}$$
$$[0\,0\,1]_H \| [0\,0\,1]_\sigma, \quad c_H = c_\sigma = 0.45\,\text{nm}$$

In spite of $a_H = c_H$, a C-centred orthorhombic cell instead of a tetragonal one has been chosen because there is no fourfold axis.

The high-resolution image of the H phase shows an *mm* symmetry (Fig. 20). Since the antiprism itself has a mirror plane perpendicular to its axis, the H phase must have the *mmm* point group and the *Cmmm* space group. From the 3^342^2 juxtaposition of hexagonal antiprisms the atom positions and their coordination numbers can be derived (Table III and Fig. 21).

Fig. 22a is the composite [0 0 1] EDP of the H phase, together with two differently oriented σ phases, and Fig. 22b is its schematic drawing with the diffraction spots of H drawn as circles and those of σ as two square crossgrids of solid and dashed lines, respectively. The five different sizes of the circles of the H phase represent the diffraction intensities calculated from the atom positions listed in Table III according to the dynamical theory of electron diffraction. They agree quite well with the observed results. The simulated image based on these atom positions also agree

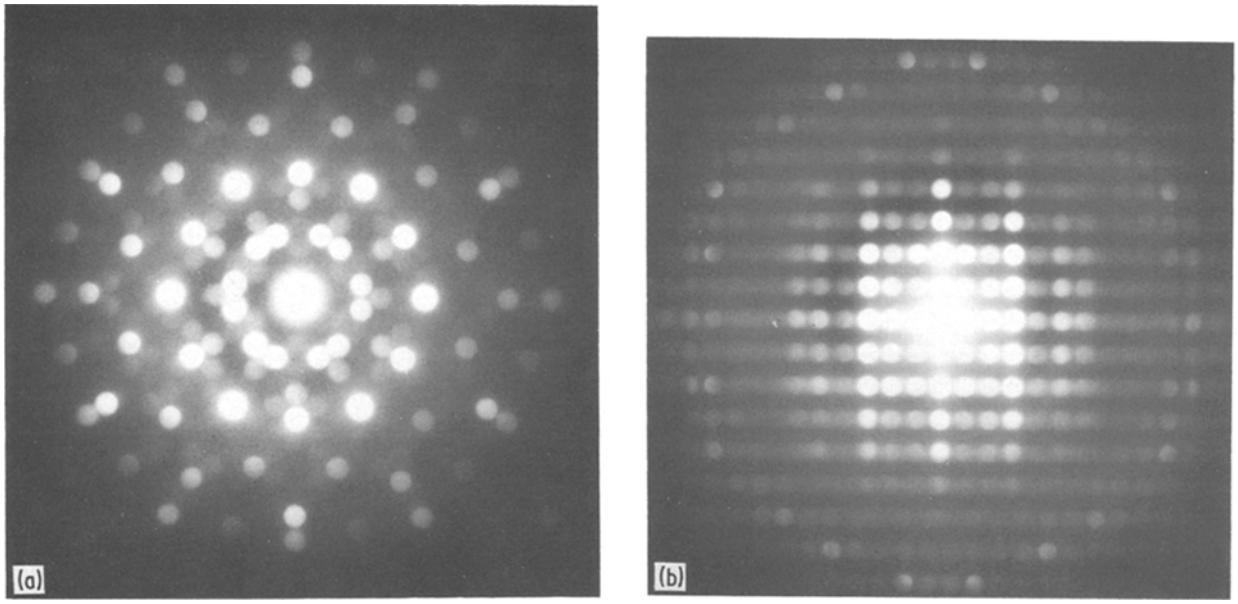

Figure 18 (a) [0 0 0 1] and (b) [1 0 $\bar{1}$ 0] CBED patterns of the F phase [49].

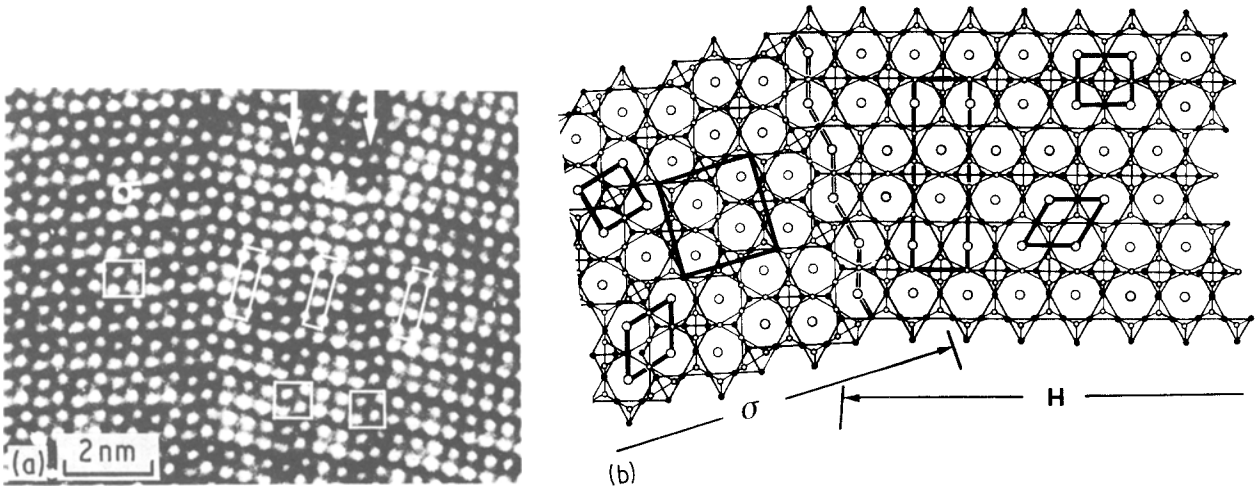

Figure 19 (a) Structural image, and (b) model of the intergrowth structure of σ and H. No disorder exists at the interphase boundary. Unit cells are outlined: Cr_3Si (small square); Zr_4Al_3 (rhombus); σ (large square); H (rectangle).

well with the observed high-resolution image as can be seen in Fig. 20.

4.1.2. F phase [35]

Fig. 23a is a high-resolution image showing the coexistence of a new F phase with the well-known σ phase. As shown in the schematical diagrams (Figs. 23c and 24), F is also composed of Cr_3Si square and Zr_4Al_3 triangular units of hexagonal antiprisms in a $3^6 + 3^2434(1:6)$ network displaying hexagonal symmetry. From the orientation relationship shown in Fig. 24, one can obtain:

$$[1\,0\,0]_F \| [1\,\bar{1}\,0]_\sigma, \quad a_F = b_F = 2^{1/2} a_\sigma = 1.25\,\text{nm}$$

$$[0\,1\,0]_F \| [1\,4\,0]_\sigma, \quad \gamma = 120^\circ$$

$$[0\,0\,1]_F \| [0\,0\,1]_\sigma, \quad c_F = c_\sigma = 0.45\,\text{nm}$$

As discussed in Section 3.3, its space group is *P6/mmm* as determined both by CBED [49] and HREM [35]. The atom positions inferred from its close relationship with the σ structure are listed in Table IV and shown in Fig. 25a.

The imaging conditions of the F phase are similar to those of the σ phase since the hexagonal antiprisms in both phases are imaged as bright dots in Fig. 23a. Fig. 25b shows the good match between the simulated and observed images.

The [0 0 1] EDP of the F phase shows a distinct *6mm* symmetry (Fig. 26a) and the calculated intensities of the $hk0$ reflections agree with the experimental results, at least as far as the twelve strong diffraction spots on the inner ring are concerned. This agrees also with the CBED pattern shown in Fig. 18a.

4.1.3. K phase [35]

A different tessellation of 3^6 and $3^2434(1:10)$ from that of the F phase has been found in the K phase coexisting also with the σ phase (see Figs. 27 and 28). Following the same procedure as in the case of H and F, the atom position (Table V) as well as the orientation relationship between K and σ have been obtained:

$$[1\,0\,0]_K \| [1\,\bar{1}\,0]_\sigma, \quad a_K = 2^{1/2} a_\sigma = 1.25\,\text{nm}$$

$$[0\,1\,0]_K \| [1\,1\,0]_\sigma, \quad b_K = 2a_\sigma \cos 14.03^\circ = 1.71\,\text{nm}$$

$$[0\,0\,1]_K \| [0\,0\,1]_\sigma, \quad c_K = c_\sigma = 0.45\,\text{nm}$$

Based on the atom positions listed in Table V the simulated image and [0 0 1] EDP were calculated and they agree well with the experimental results (Figs. 27 and 29). It is of interest to note that although the K phase has a *Pmmm* space group, it has 12 strong $hk0$ diffraction spots lying almost symmetrically on the outer ring in Fig. 29. This comes

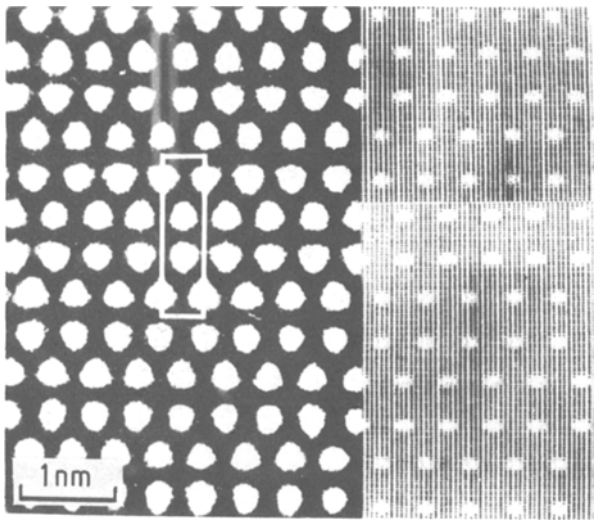

Figure 20 Each bright dot of the structural image of the H phase (middle) corresponds to a pentagonal antiprism (left). The unit cell of H is outlined.

TABLE III Crystallographic data for the H phase *Cmmm*-D_{2h}^{19}; $a = 0.45$, $b = 1.75$, $c = 0.45$ nm; $z = 30$. Atomic coordinates: $000 + \frac{1}{2}\frac{1}{2}0$. $Z = \frac{1}{4}$.

Type	Number	Position	Coordination number	Cordinates
A	2	2(a)	12	000
B	4	4(e)	12	$\frac{1}{4}\frac{1}{4}0$
C	4	4(i_c)	15	$0\,y_C\,0$ $y_C \simeq 0.2892$
D	4	4(i_d)	14	$0\,y_D\,0$ $y_D \simeq 0.4206$
E	4	4(j)	12	$0\,y_E\,\frac{1}{2}$ $y_E \simeq 0.3677$
F	4	4(h)	14	$X_F\,0\,\frac{1}{2}$ $x_F \simeq 0.2000$
G	8	8(n)	14	$0\,y_G\,Z$ $y_G \simeq \frac{1}{8}$

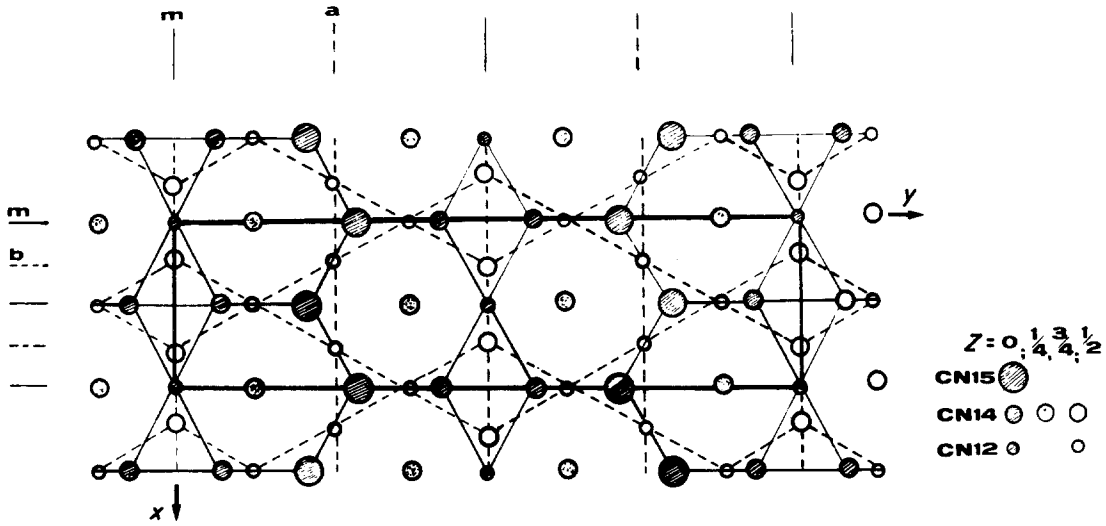

Figure 21 [0 0 1] projection of the H structure.

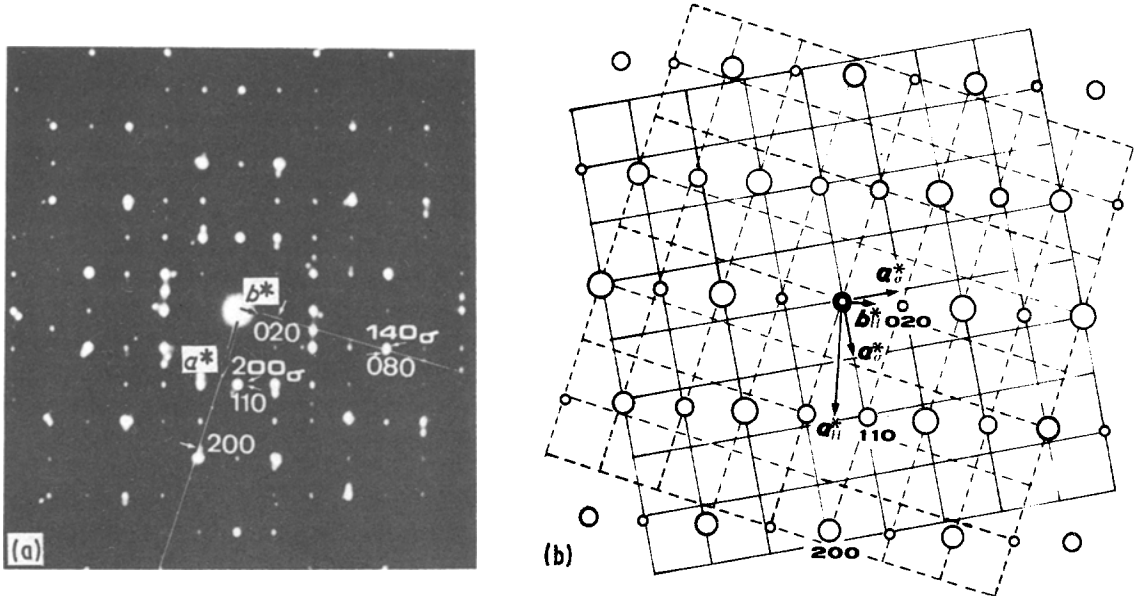

Figure 22 (a) A composite [0 0 1] EDP of H and two σ domains, and (b) the indexing scheme in which the H spots are shown as circles of different sizes according to their calculated intensities. The two crossgrids in solid and dashed lines correspond to the spot patterns of the two σ domains.

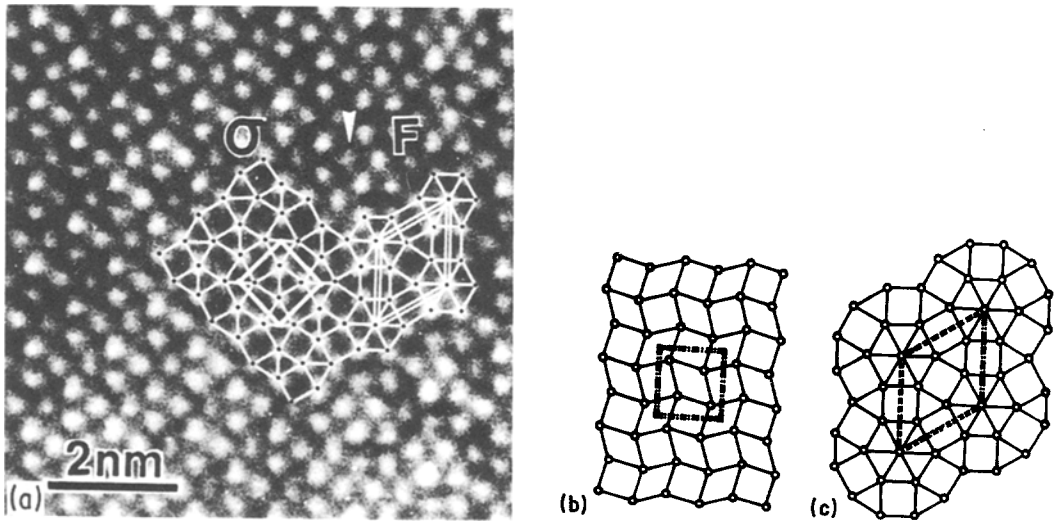

Figure 23 (a) [0 0 1] structural image showing the intergrowth of σ and F whose unit cells and secondary networks are outlined. (b) $3^2\,4\,3\,4$ network of σ. (c) $3^6 + 3^2\,4\,3\,4$ network of F.

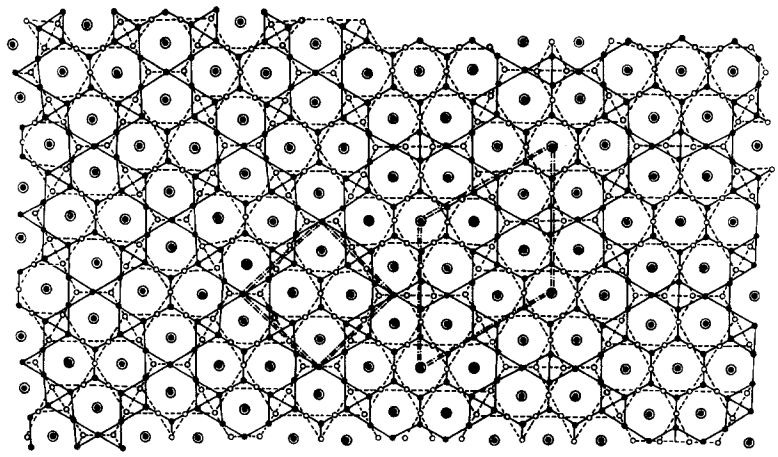

Figure 24 [0 0 1] structure model of the intergrowth structure of σ and F.

from the hexagonal antiprism which is the fundamental building block of the K structure. This will be further discussed in Section 6.

4.1.4. J phase [35]

The structure of the J phase $[3^6 + 3^3 4^2 (1:2)]$ coexisting with the F phase is rather similar to that of the H phase with a $3^3 4^2$ juxtaposition of hexagonal antiprisms. Both have orthorhombic unit cells and the same a and c parameters, and their b parameters (b_H = 1.75 nm, b_K = 1.25 nm) are in simple proportion. The atom positions inferred from Fig. 30 are listed in Table VI from which the simulated image as an inset in Fig. 30 is calculated.

4.2. Laves and μ related phases: C and C_1

During the observation of high-resolution images of the C14 Laves phase, a periodic intergrowth of single slabs of the C14 Laves and μ phases has often been encountered. According to the classification of pentagonal tcp phases stated in Section 2.4, this is the third-order C structure shown in Fig. 10h. This structure is isomorphous with the C-silicide, $V_2(Co_{0.57}Si_{0.43})_3$ [37, 38]. Owing to its very small particle size, it is difficult to carry out X-ray microanalysis of this C phase. The coexisting C14 Laves phase has a composition like $(Fe_{0.16}Cr_{0.10}Ni_{0.06})_2(Mo_{0.14}Ti_{0.10}Al_{0.10}W_{0.2})$ containing no silicon, and it is presumed that the C phase particles embedded in the Laves phase may also contain no or very little silicon.

4.2.1. C phase [52]

Fig. 31a is the structural image showing the intergrowth of the C phase and the C14 Laves phase (L in Fig. 31a). Just as the structure of H is inferred from that of the σ phase, the structure of the C phase can equally well be derived from that of the C14 Laves phase. Assuming each bright dot represents a pentagonal antiprism as is the case with the C14 Laves phase, the structure of the C phase is shown in Fig. 31b consisting alternately of single slabs of the C14 Laves and μ phases. It has a B-centred monoclinic unit cell and its space group is *B2/m* with a two-fold axis parallel and a mirror plane perpendicular to the c axis. The atom positions are listed in Table VII. The orientation relationship between the C and C14 Laves phase is:

$$(0\,1\,0)_C \| (1\,\bar{1}\,\bar{1})_L$$

$$[1\,0\,0]_C \| [1\,\bar{1}\,2]_L$$

$$[0\,0\,1]_C \| [1\,1\,0]_L$$

TABLE IV Crystallographic data of the F phase *P6/mmm*; $a = b = 1.25$, $c = 0.45$ nm, $\gamma = 120°$, $Z = 52$

Number	Position	Coordination number	Coordinates		
2	2(d)	15	$\frac{1}{3}$	$\frac{2}{3}$	$\frac{1}{2}$
2	2(e)	14	0	0	$\frac{1}{4}$
6	6(j_1)	15	0.223	0	0
6	6(j_2)	14	0.444	0	0
6	6(k)	12	$\frac{1}{3}$	0	$\frac{1}{2}$
6	6(l)	12	0.390	0.780	0
6	6(m_1)	12	0.112	0.223	$\frac{1}{2}$
6	6(m_2)	14	0.444	0.888	$\frac{1}{2}$
12	12(o)	14	0.223	0.446	$\frac{1}{4}$

TABLE V Crystallographic data of the K phase *Pmmm*; $a = 1.25$, $b = 1.71$, $c = 0.45$ nm, $Z = 82$

Number	Position	Coordination number	Coordinates		
1	1(e)	12	0	$\frac{1}{2}$	0
1	1(h)	12	$\frac{1}{2}$	$\frac{1}{2}$	$\frac{1}{2}$
2	2(i_1)	15	0.220	0	0
2	2(i_2)	14	0.442	0	0
2	2(j)	12	$\frac{1}{3}$	0	$\frac{1}{2}$
2	2(k)	15	0.392	$\frac{1}{2}$	0
2	2(n_1)	12	0	0.143	$\frac{1}{2}$
2	2(n_2)	15	0	0.430	$\frac{1}{2}$
2	2(o)	12	$\frac{1}{2}$	0.143	0
2	2(p_1)	14	$\frac{1}{2}$	0.072	$\frac{1}{2}$
2	2(p_2)	15	$\frac{1}{2}$	0.216	$\frac{1}{2}$
2	2(q)	14	0	0	$\frac{1}{4}$
4	4(u)	14	0	0.286	$\frac{1}{4}$
4	4(v)	14	$\frac{1}{2}$	0.358	$\frac{1}{4}$
4	4(x)	14	0.167	$\frac{1}{2}$	$\frac{1}{4}$
4	4(y_1)	12	0.085	0.376	0
4	4(y_2)	15	0.110	0.143	0
4	4(y_3)	14	0.220	0.286	0
4	4(y_4)	14	0.277	0.358	0
4	4(y_5)	12	0.415	0.253	0
4	4(z_1)	12	0.167	0.072	$\frac{1}{2}$
4	4(z_2)	12	0.167	0.216	$\frac{1}{2}$
4	4(z_3)	14	0.167	0.358	$\frac{1}{2}$
4	4(z_4)	14	$\frac{1}{3}$	0.286	$\frac{1}{2}$
4	4(z_5)	12	$\frac{1}{3}$	0.428	$\frac{1}{2}$
8	8(α)	14	$\frac{1}{3}$	0.143	$\frac{1}{4}$

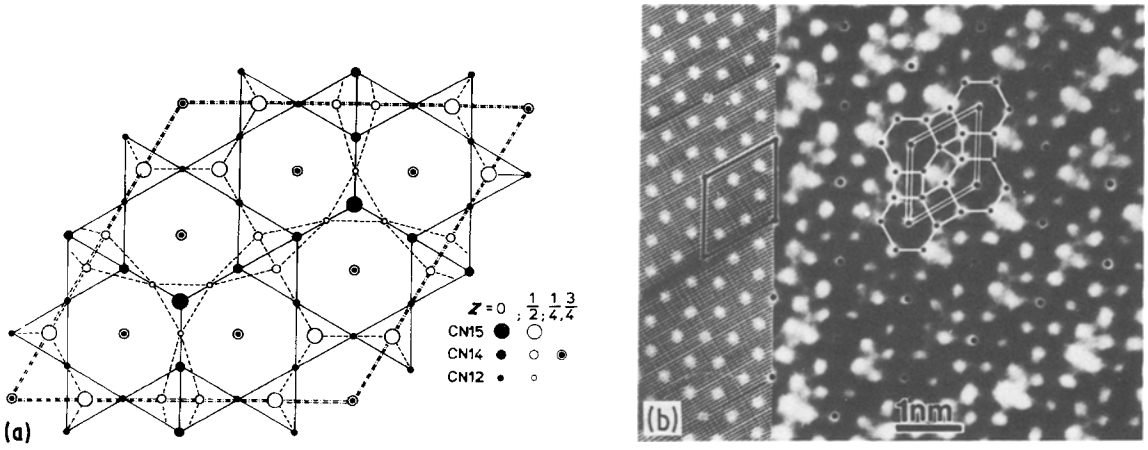

Figure 25 (a) [0 0 1] structure model, and (b) high-resolution and simulated (t = 6.8 nm and Δf = −67 nm) images of F.

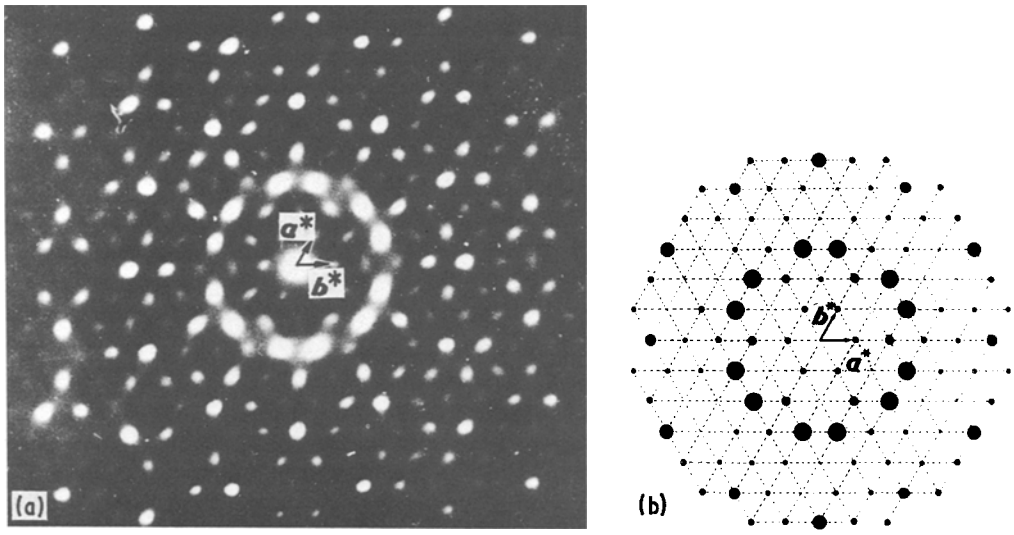

Figure 26 (a) [0 0 1] EDP, and (b) calculated $hk0$ intensities of F.

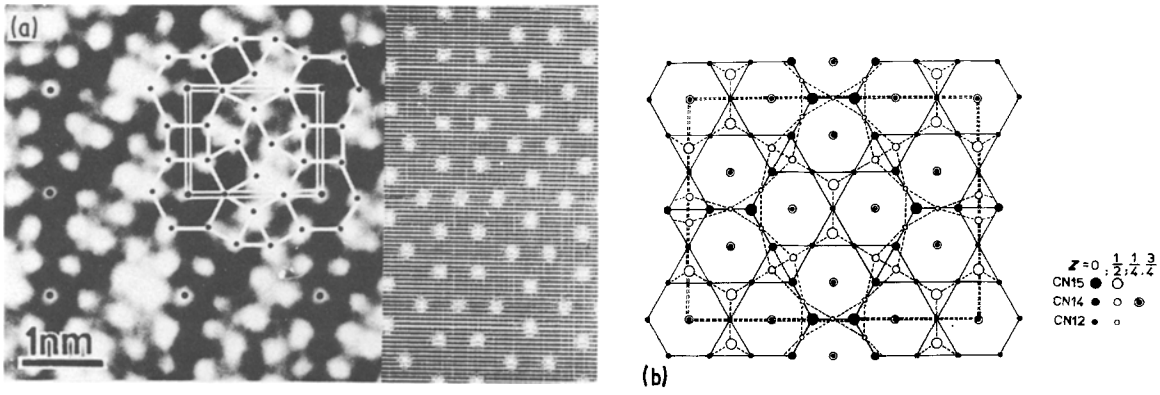

Figure 27 [0 0 1] structural image (left) compared with a simulated one (right, t = 6.8 nm and Δf = −67 nm) of K based on the structure model shown in (b).

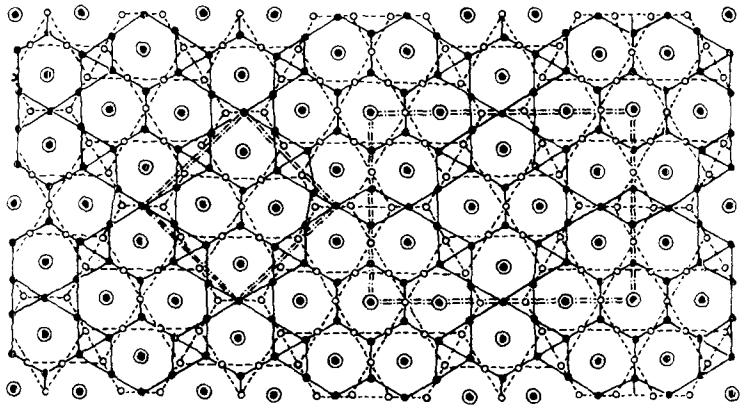

Figure 28 Structure model of the intergrowth structure of σ and K whose unit cells are outlined.

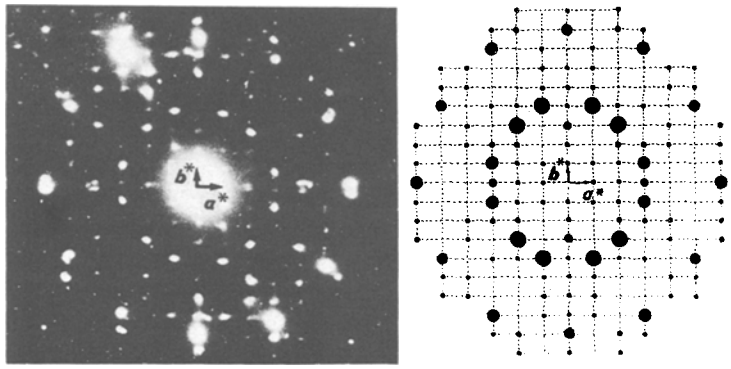

Figure 29 (a) [0 0 1] EDP, and (b) calculated $hk0$ intensities of K.

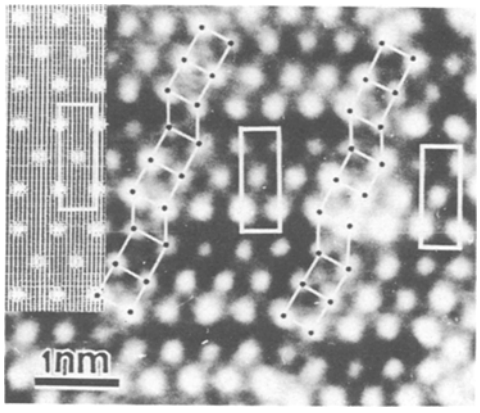

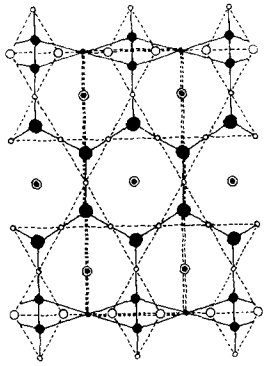

Figure 30 [0 0 1] structural image (right) compared with a simulated image (shown as an inset, $t = 6.8$ nm and $\Delta f = -67$ nm) of J based on its structure model shown on the left.

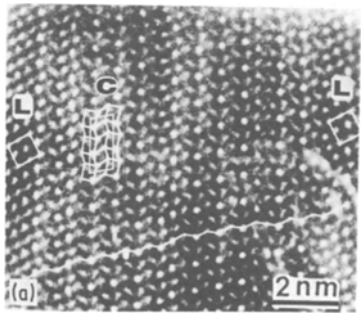

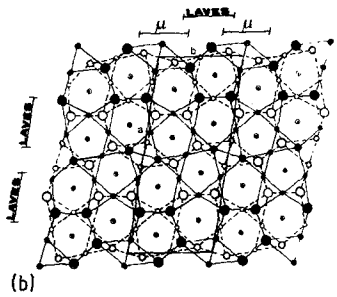

Figure 31 (a) Structural image shows the intergrowth of C14 Laves and C phases. (b) C consists alternatively of single slabs of C14 Laves and μ phases.

TABLE VI Crystallographic data of the J phase *Pmmm*; $a = 0.45$, $b = 1.25$, $c = 0.45$ nm, $Z = 22$

Number	Position	Coordination number	Coordinates		
1	1(a)	12	0	0	0
1	1(g)	12	0	$\frac{1}{2}$	$\frac{1}{2}$
2	2(j)	14	0.259	0	$\frac{1}{2}$
2	2(m)	15	0	0.387	0
2	$2(o_1)$	14	$\frac{1}{2}$	0.060	0
2	$2(o_2)$	15	$\frac{1}{2}$	0.280	0
2	2(p)	12	$\frac{1}{2}$	0.167	$\frac{1}{2}$
2	2(t)	14	$\frac{1}{2}$	$\frac{1}{2}$	$\frac{1}{4}$
4	4(u)	14	0	0.167	$\frac{1}{4}$
4	4(z)	12	0.259	$\frac{1}{3}$	$\frac{1}{2}$

and the lattice parameters of the C phase are: $a = 1.78$, $b = 0.77$, $c = 0.47$ nm, $\gamma = 99°$, $Z = 50$.

Fig. 32 shows the observed and simulated [0 0 1] images of the C phase compared with its structure model. The monoclinic unit cell of the C phase can also be identified in its [0 0 1] EDP shown in Fig. 33, in which all the $hk0$ reflections with h = odd are extinctions confirming the B-centred lattice. The calculated EDP is shown in Fig. 33b in which there are ten strong diffraction spots lying symmetrically on the outermost ring. This is the manifestation of the parallel arranged pentagonal antiprisms which will be further discussed in Section 6.

4.2.2. C_1 phase [36]

Fig. 34a is the high-resolution image of a second new phase, called C_1, found in intergrowth with the C or C14 Laves phases and it consists alternately of a single slab of the μ phase together with a double slab of the C14 Laves phase. The structure of this phase is shown schematically in Fig. 34b and it is clear that it also has a B-centred monoclinic unit cell with a = 1.78, $b = 1.22$, $c = 0.47$ nm, $\gamma = 115°$ and $Z = 56$. Its space group is also *B2/m* and the atom positions are listed in Table VIII. The orientation relationships among C_1, C and C14 Laves phases are:

$$(0\,1\,0)_{C_1} \| (0\,1\,0)_C \| (1\,\bar{1}\,\bar{1})_L$$

$$[1\,0\,0]_{C_1} \| [1\,0\,0]_C \| [1\,\bar{1}\,2]_L$$

$$[0\,0\,1]_{C_1} \| [0\,0\,1]_C \| [1\,1\,0]_L$$

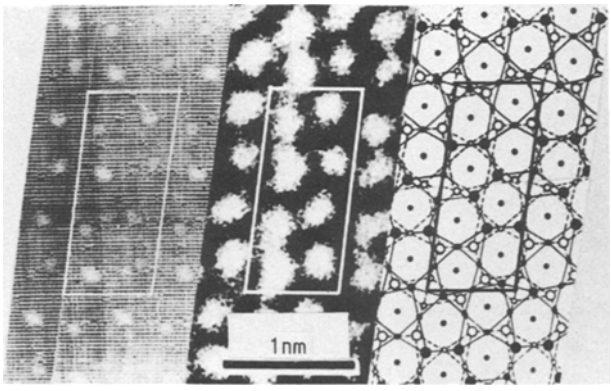

Figure 32 [0 0 1] structural image of C, in which each bright dot represents a pentagonal antiprism. There is good agreement with the simulated image ($t = 5$ nm and $\Delta f = -67$ nm).

TABLE VII Crystallographic data of the C phase *B2/m*; $a = 1.78$, $b = 0.77$, $c = 0.47$ nm, $\gamma = 99°$, $Z = 50$

Number	Position	Coordinates		
		x	y	z
1	4(i)	0.048	0.367	0.000
2	4(i)	0.208	0.562	0.000
3	4(i)	0.208	0.932	0.000
4	4(i)	0.473	0.817	0.000
5	4(i)	0.069	0.981	0.000
6	4(i)	0.287	0.267	0.000
7	4(i)	0.347	0.543	0.000
8	4(i)	0.375	0.042	0.000
9	4(i)	0.160	0.226	0.250
10	4(i)	0.088	0.695	0.250
11	4(i)	0.160	0.226	0.750
12	4(i)	0.088	0.095	0.750
13	2(c)	0.000	0.500	0.000

4.3. Resumé

The main crystallographic data of the six new tcp phases are summarized in Table IX [53] which is an addition to Table I in which the main data of the tcp phases already known are listed. These phases have been discovered in commercial superalloys in intimate intergrowth with either the σ or the C14 Laves phases. They seldom grow to a size exceeding 0.1 μm and this may be the reason why they have not been detected before by either X-ray diffraction or conventional TEM methods. This is the field where HREM can be used most advantageously as shown by our discovery of the six new phases and also by the rich microdomain structures to be presented below in Section 5.

A combination of HREM and SAD or even better CBED will be very effective in the study of ultrafine structures of alloys. We have made a little excursion into the field of superalloys and the reward is indeed great. It is our firm belief that this is a general case rather than an exception because most metallic phases will have fine structures and the problem is whether or not one can detect them. With the improvement of the microbeam analytical techniques, more new metallic phases will be found in various alloys.

5. Microdomain structures

Many planar faults exist in tcp phases and sometimes they are called stacking faults in the literature [17, 18], although it is not always possible to make layer stacking analysis of these planes. On the other hand, this interface can very well be considered as a domain boundary and the two regions separated by this interface are either translation or rotation domains. Furthermore, in the case of tcp phases, the domain boundary is, in fact, nothing but a different tessellation of the pentagonal or hexagonal antiprisms. In this sense, the domain boundary is very often a very narrow region of another tcp phase belonging to the same class. With the exception of the basal faults of the pentagonal tcp phases, such as the C14 Laves, μ, etc, which are real stacking faults, all other planar faults are treated as domain boundaries.

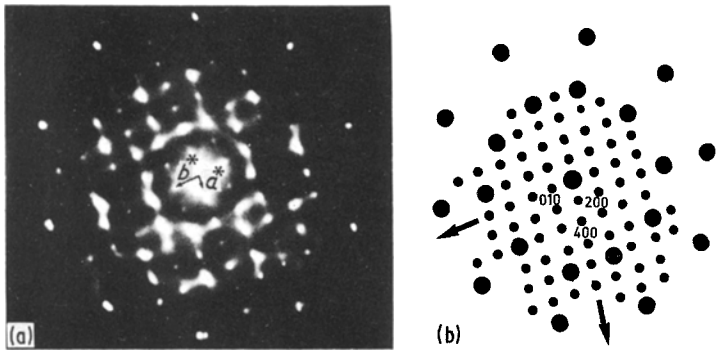

Figure 33 (a) [0 0 1] EDP, and (b) calculated $hk0$ intensities of C in which the 10 strong diffraction spots on the outermost ring come from parallel oriented icosahedra.

5.1. σ phase related domain structures

5.1.1. Domain structures in σ and H phases [34, 54, 55]

The general appearance of the domain structures in σ and H phases is shown in Fig. 35 in which the unit cells in various domains are outlined. The domain boundaries, marked with arrows in Fig. 35, sometimes have kinks (K) and interesections (I). Besides the translation domains in both σ and H phases, no less than five H rotation domains can be found in this image. Microdomains are only a few nm in size (Fig. 36).

5.1.1.1. Translation domain boundary. From the model of the intergrown σ–H structure (Fig. 19) it is clear that the interface, outlined with double lines, is either $(1\,0\,0)_\sigma$ or $(1\,1\,0)_H$ and the zigzag slab of hexagonal antiprisms belongs to both the σ and H phases. This is the reason why the boundary structure is perfect and the intergrowth of these two phases occurs very frequently. Fig. 37a is the high-resolution image of (1 0 0) planar faults in σ and there are three narrow H ribbons consisting of three zigzag slabs in each of them (one of them is shown schematically in Fig. 37b). Fig. 38a is the high-resolution image of $(1\,\bar{1}\,0)$ planar faults or translation domain boundaries in H which can be considered as σ slabs (outlined in Fig. 38a) or differently oriented H slabs (rotation H domains) as shown in Fig. 38b.

5.1.1.2. Intersection of translation domain boundaries. When two translation domain boundaries intersect, a new tcp structure will appear at the intersection. In Fig. 39 a $(1\,0\,0)_\sigma$ boundary intersects a $(0\,1\,0)_\sigma$ boundary resulting in a Zr_4Al_3 domain at the junction, while in Fig. 40a $(1\,\bar{1}\,0)_H$ and $(\bar{1}\,\bar{1}\,0)_H$ domain boundaries intersect either at 30° (top left) or 150° (both tcp left and bottom right). The latter was denoted as a kink (K) in Fig. 35 and Zr_4Al_3 slab forms at the kink in one of the H domains (indicated by arrows in

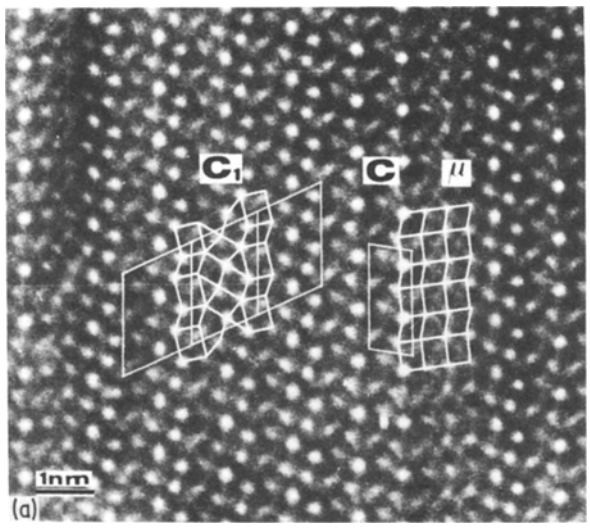

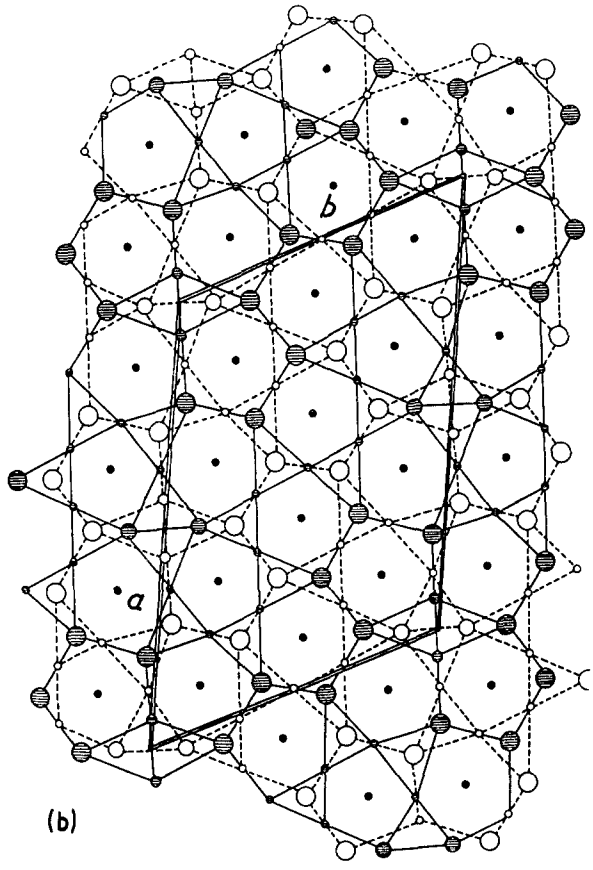

Figure 34 (a) [0 0 1] structural image of the intergrowth structure of C and C_1 in which both unit cells as well as the Zr_4Al_3 and $MgCu_2$ units are outlined. (b) [0 0 1] projection of the structure model of C_1.

TABLE VIII Crystallographic data of the C_1 phase $B2/m$; $a = 1.78$, $b = 1.22$, $c = 0.47$ nm, $\gamma = 115°$, $Z = 76$

Number	Position	Coordinates		
		x	y	z
1	4(i)	0.057	0.252	0.000
2	4(i)	0.239	0.421	0.000
3	4(i)	0.239	0.050	0.000
4	4(i)	0.345	0.308	0.000
5	4(i)	0.050	0.618	0.000
6	4(i)	0.480	0.895	0.000
7	4(i)	0.070	0.013	0.000
8	4(i)	0.355	0.975	0.000
9	4(i)	0.215	0.821	0.000
10	4(i)	0.208	0.632	0.000
11	4(i)	0.355	0.660	0.660
12	4(i)	0.480	0.685	0.000
13	4(i)	0.181	0.204	0.250
14	4(i)	0.181	0.204	0.750
15	4(i)	0.403	0.151	0.250
16	4(i)	0.403	0.151	0.750
17	4(i)	0.394	0.525	0.250
18	4(i)	0.394	0.525	0.750
19	2(c)	0.500	0.500	0.000

Fig. 40a and also shown schematically in Fig. 40b).

5.1.1.3. Rotation domains. In the structure of the σ phase there are two differently oriented Cr_3Si square units with a relative rotation of about 28° between them (see Figs. 39 and 41). If this rotation occurs in different senses, two differently oriented σ domains will result and very often a wedge-form H domain occurs between these two σ rotation domains (Fig. 41). Since the H structure also consists of square Cr_3Si units, it is natural to expect that 28° rotation domains will also exist in the H phase. Fig. 42a shows a fan-like image of successive rotation domains of H with zigzag domain boundaries which, in fact, are σ slabs (Fig. 42b). It is thus clear that the domain boundary in σ is a narrow region of H and *vice versa*, no matter whether they are translation or rotation domains. This explains the frequent occurrence of the σ–H intergrown structure.

5.1.2. Domain structure in F, K and J phases [35]

As mentioned in Section 4.1, these phases have a common 3^6 unit as well as the close related units of 3^2434 or 3^342. They intergrow easily and in each one of these phases there are also translation and rotation domains. Fig. 43 shows their intergrown structure as

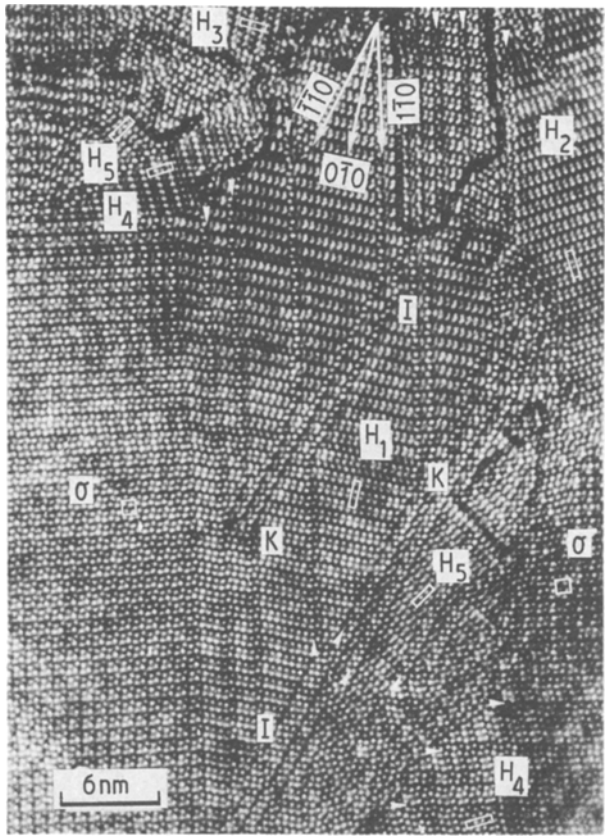

Figure 35 General mosaic appearance of σ and H domain structure (H_1 to H_5 are rotation domains of H). Domain boundaries on $(0\,1\,0)_H$, $(1\,1\,0)_H$ and $(\bar{1}\,\bar{1}\,0)_H$ sometimes cross each other forming intersections (I) and kinks (K).

well as the translation and rotation domains of the J phase. Even in this case there is no disorder at all at the domain boundaries as shown at least by the arrangement of the hexagonal antiprisms in Fig. 43b. These domains of σ-related structures are the result of the (1 1 0) planar faults in the σ phase, just as H domains are that of the (1 0 0) faults.

5.2. Laves phase related domain structures [56–58]

Figs. 44 and 45 show the general appearance of the domain structure in the C14 Laves and μ phases, respectively, where the domain boundaries are marked with arrows. In the former case, translation domain boundaries occur on (0 0 1), $(1\,\bar{1}\,0)$ and $(1\,\bar{1}\,\bar{1})$ planes denoted by B, V and T, respectively, in Fig. 44. In the latter case, translation domain boundaries occur on (0 0 1), $(\bar{1}\,1\,1)$ and $(1\,\bar{1}\,2)$ planes and one rotation domain boundary on $(1\,\bar{1}\,2)$ denoted by R in Fig. 45. The (0 0 1) domain boundary is, in fact, a

TABLE IX Crystal structrures of new phases

Phase	Space group	Network of the second layers		Lattice constants (nm)				Atoms per unit cell
				a_0	b_0	c_0		
H	*Cmmm*	$3^3\,4^2$		0.45	1.75	0.45		30
F	*P6/mmm*	$3^6 + 3^2434$	(1:6)	1.25	1.25	0.45		52
K	*Pmmm*	$3^6 + 3^2434$	(1:10)	1.25	1.71	0.45		82
J	*Pmmm*	$3^6 + 3^3\,4^2$	(1:2)	0.45	1.25	0.45		22
C	*B2/m*	$3^54 + 3\,3^24$	(1:1)	1.78	0.77	0.47	$\beta = 99°$	50
C_1	*B2/m*	$3^43^2 + 3^54 + 3\,3^24$	(1:1:1)	1.78	1.22	0.47	$\beta = 115°$	76

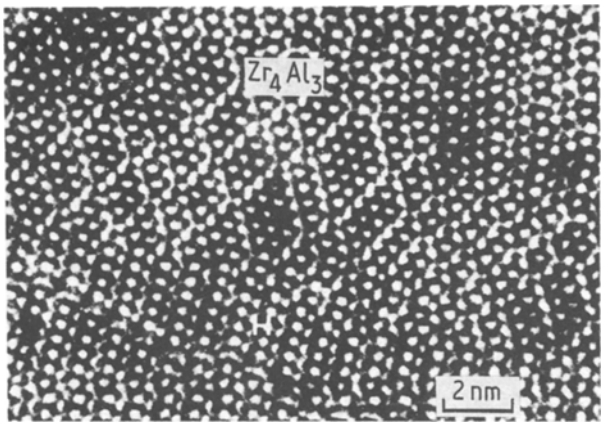

Figure 36 Microdomains of only a few nanometres in size.

stacking fault or another stacking variant and this will not be included in the following discussion.

5.2.1. Translation domains

5.2.1.1. $(1\,\bar{1}\,\bar{1})$ domain boundary. Fig. 46 is a schematic diagram of the $(1\,\bar{1}\,\bar{1})$ and $(1\,\bar{1}\,0)$ boundary structure in the C14 Laves phase projected on $(1\,1\,0)$ in which the unit cells are outlined by double lines and the boundary region by solid and dashed lines. Let us examine the $(1\,\bar{1}\,\bar{1})$ boundary first. At the *s* side of an $MgCu_2$ unit of the central C14 Laves domain, another $MgCu_2$ unit in twin position is attached to it, whereas at the *l* side, a Zr_4Al_3 unit is added. At this domain boundary, alternate $MgCu_2$ and Zr_4Al_3 units sharing the *s* side from a slab of the μ phase (Fig. 46). Such μ slabs have been found as the domain boundary structure of translation domains in the C14 Laves phase and one of them is outlined in Fig. 47.

Fig. 48 is a schematic diagram of the $(\bar{1}\,1\,1)$ and $(1\,\bar{1}\,2)$ boundary structure in the μ phase projected on $(\bar{1}\,\bar{1}\,0)$ in which the boundary itself is outlined. Now at the *l* side of the Zr_4Al_3 unit of the central μ domain, an $MgCu_2$ unit is added, whereas at the *s* side of an $MgCu_2$ unit, another unit in the twin position is attached. This is the reverse formation mechanism to that discussed above in connection with the $(1\,\bar{1}\,\bar{1})$ translation domain boundary of the C14 Laves phase. In other words, this is a slab of C14 Laves phase between two parallel μ domains. Such an image is shown in Fig. 49 in which both the μ unit cells and the boundary structure are outlined.

Just as σ and H can intergrow intimately, so do the C14 Laves and μ phases, and this explains the abundance of microdomains in these phases as shown in Figs. 44 and 45.

5.2.1.2. $(1\,\bar{1}\,0)_L$ domain boundary. The schematic diagram of such a boundary is shown on the right in Fig. 46 in which the $MgCu_2$ and Zr_4Al_3 units of the boundary make contact with the $MgCu_2$ units of the C14 Laves phase only at thes sides. As a consequence of this, short segments of C14 Laves and μ phases occur alternately in a direction at an angle of 71° to the $(1\,\bar{1}\,\bar{1})_L$ boundary. In other words, the $(1\,\bar{1}\,\bar{1})_L$ and $(1\,\bar{1}\,0)_L$ boundary structures belong to the same type but oriented differently. Such a $(1\,\bar{1}\,0)$ boundary structure is shown in Fig. 50 where the rectangular Zr_4Al_3 units have two different orientations because the *s* side of the $MgCu_2$ twin units in the C14 Laves phase also has different orientations. This high-resolution image shows the frequent occurrence of this $(1\,\bar{1}\,0)$ boundary.

5.2.1.3. Intersection of domain boundaries. In the case of C14 Laves phase, when a $(1\,\bar{1}\,\bar{1})$ domain boundary intersects a $(1\,\bar{1}\,0)$ boundary, as shown in Fig. 51, three layers of cubic ABC stacking of the C15 Laves phase appear on the convex side of this intersection.

5.2.2. Rotation domains

Fig. 52a is the high-resolution image of two differently oriented μ domains in which a zigzag slab of pentagonal antiprisms at the boundary is outlined, see also Fig. 52b. A characteristic of this $(1\,\bar{1}\,2)_\mu$ boundary is the fact that only the *l* sides of Cr_3Si and Zr_4Al_3 units are used to form this boundary which is identical to the μ slabs in both domains. Therefore, there are

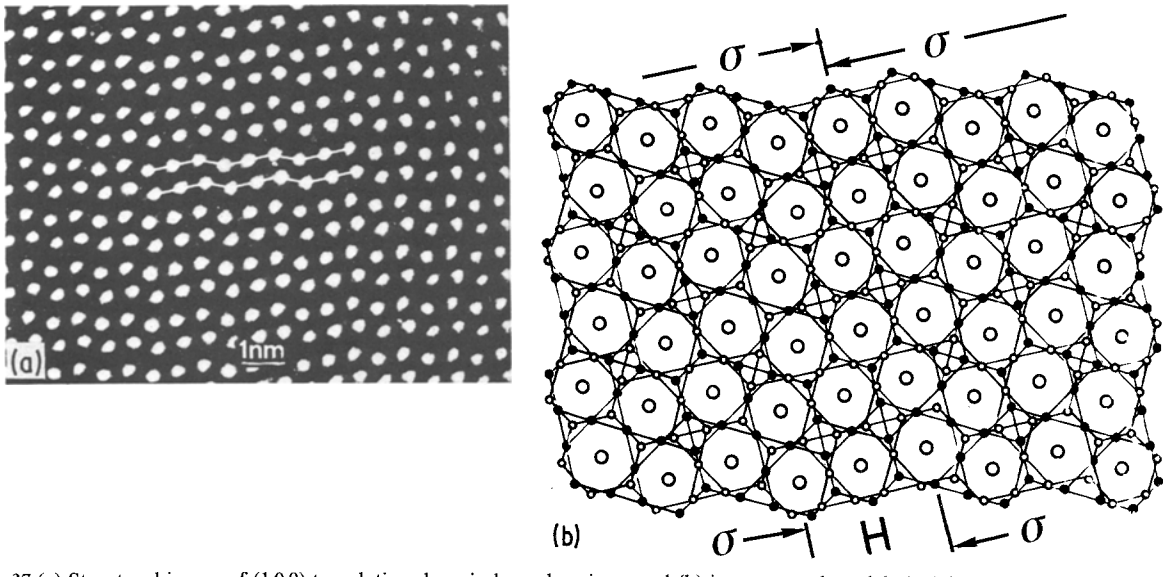

Figure 37 (a) Structural image of (1 0 0) translation domain boundary in σ, and (b) its structural model. A slab of H phase appears at this boundary.

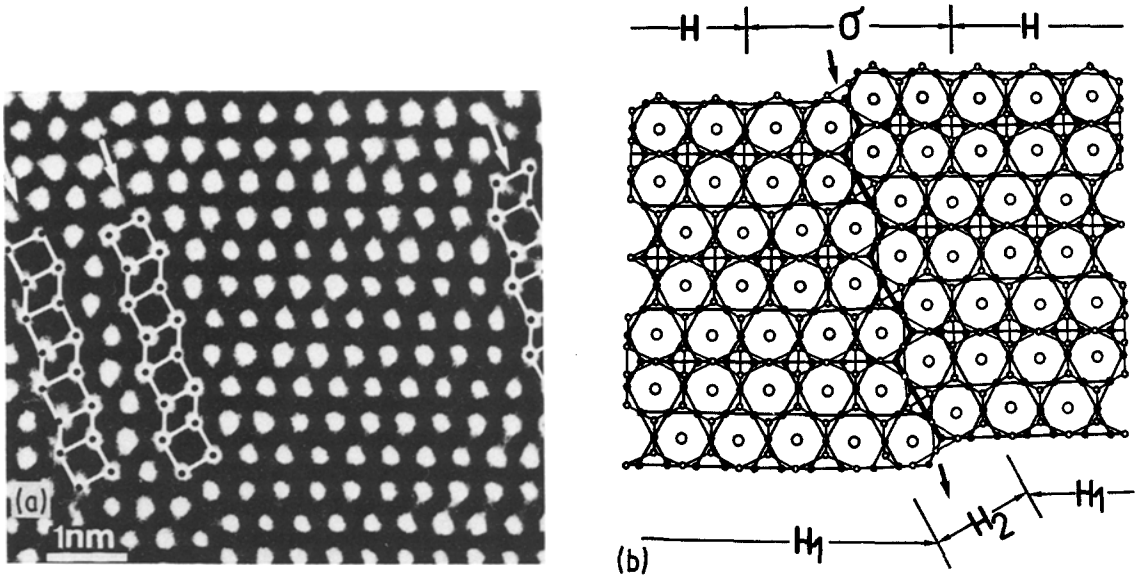

Figure 38 (a) Structural image of (1 1 0) translation domain boundary in H, and (b) its structure model. A slab of σ or a differently oriented H appears at this boundary.

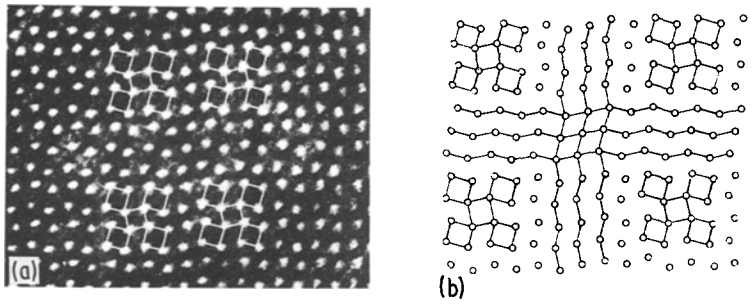

Figure 39 Structural image of an intersection of (1 0 0) and (0 1 0) domain boundaries in σ, and (b) its schematic diagram. A small domain of Zr_4Al_3 forms at this intersection.

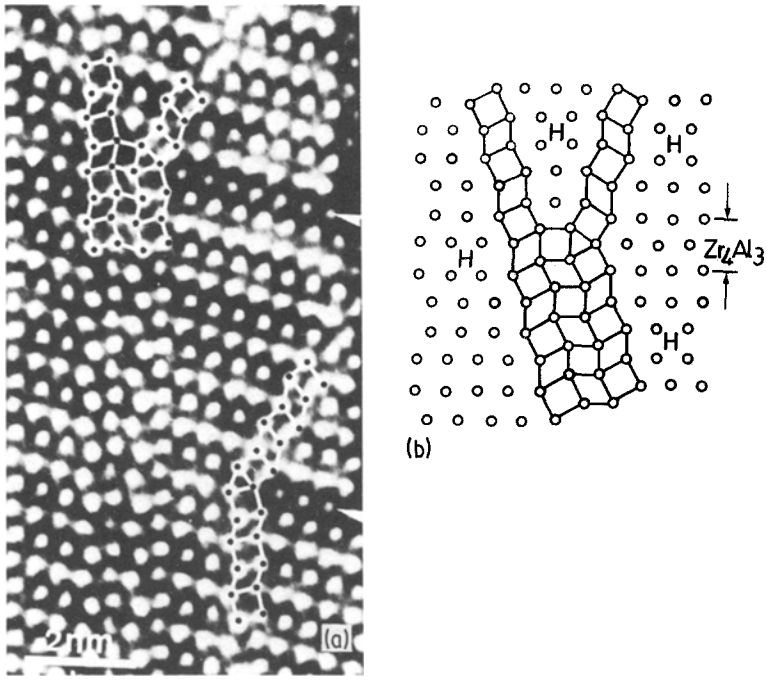

Figure 40 (a) Structural image of an intersection of translation domain boundaries in H, and (b) its schematic diagram.

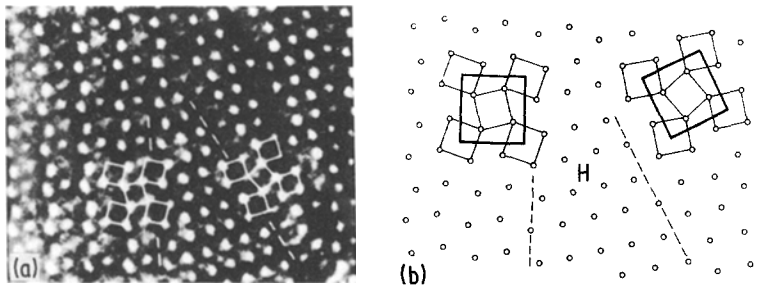

Figure 41 (a) Structural image of two rotation domains of σ with a wedge form of H, and (b) its schematic diagram.

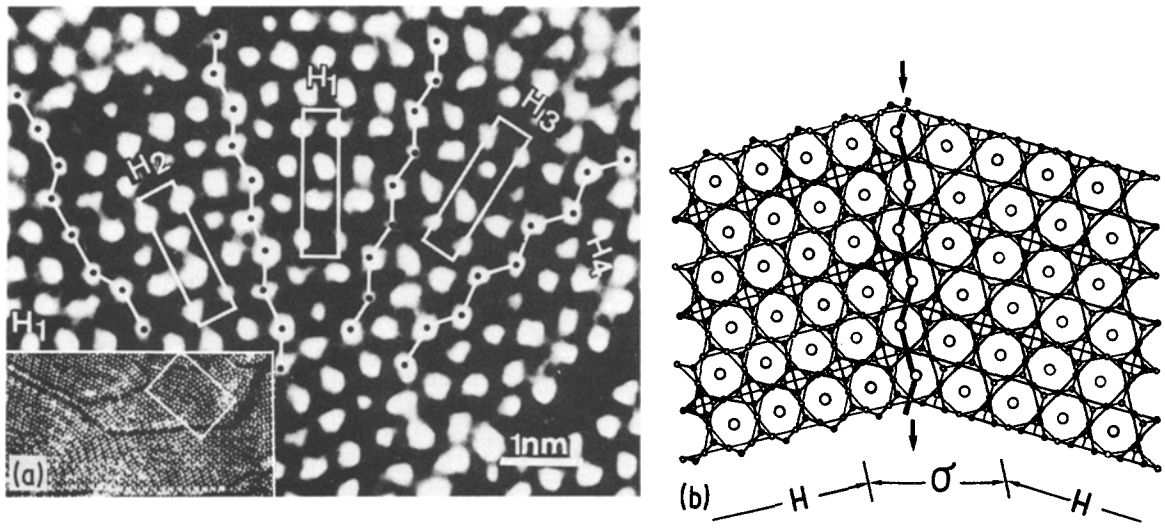

Figure 42 (a) Structural image of fan-like successive rotation domains of H, and (b) its structure model. σ appears also at the rotation domain boundary.

two differently oriented μ slabs coexisting at the $(1\,\bar{1}\,2)_\mu$ boundary and they together form a slab of the W_2FeSi phase which is a third-order structure of the pentagonal class of tcp structures (Fig. 10j). Such a differently oriented μ slab or the W_2FeSi slab also exists at the translation domain boundary between two parallel μ domains (see Fig. 48).

Rotation domains in the C14 Laves phase have also been observed [52]. It has already been dicussed in connection with the $(1\,\bar{1}\,0)$ boundary of the C14 Laves phase that two differently oriented L domains can exist (Fig. 46). However, the configuration of the arrangement of pentagonal antiprisms is rather complicated and we shall not go into detail here. In the high-resolution image of a microdomain structure of many coexisting pentagonal tcp phases, there are at least three differently oriented C14 Laves domains denoted by L, L′ and L″ in Fig. 53.

6. Long-range orientation order of antiprisms [53, 59, 60]

From the presentation above it becomes clear that not only the new tcp structures but also the various domain structures can very well be accounted for by the different tessellation of pentagonal or hexagonal antiprisms. There is no doubt that all these antiprisms are parallel, having their five-fold or six-fold axes in the same direction. But how about the orientation of

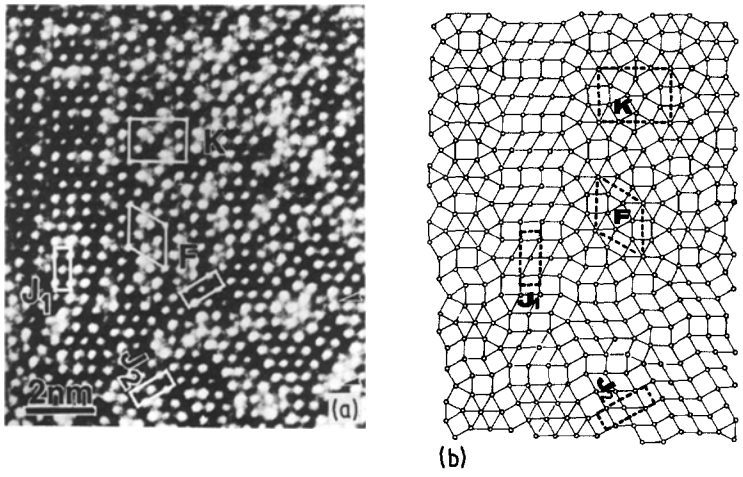

Figure 43 (a) Structural image of an intergrowth structure of K, F and J (two different orientations), and (b) its schematic diagram.

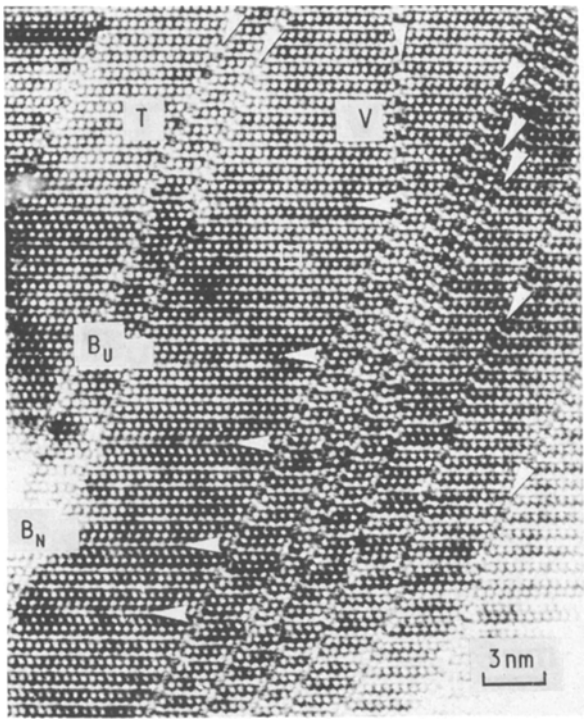

Figure 44 General mosaic appearance of domain structure in C14 Laves phase. Arrows mark the domain boundaries on (0 0 1), (1 $\bar{1}$ 0) and (1 $\bar{1}$ $\bar{1}$) denoted by B_U ($MgCu_2$ type) and B_N ($MgNi_2$ type), V and T, respectively.

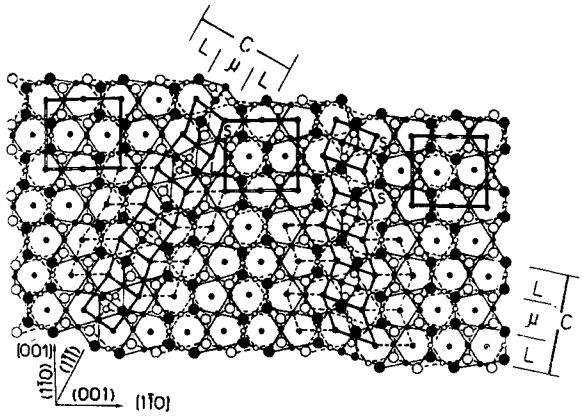

Figure 46 Structure model of translation domain boundary on (1 $\bar{1}$ $\bar{1}$) and (1 $\bar{1}$ 0) in C14 Laves phase (L). On the left, the boundary is a slab with *–s–l–s–l–* separations between pentagonal antiprisms. On the right, it is a C segment at 71° to the C slab on $(1\,\bar{1}\,\bar{1})_L$.

these antiprisms? Could they tolerate a certain relative rotation around the pentagonal or hexagonal axis in the rotation domains?

Fig. 53 shows the "mosaic" appearance of a great number of microdomains of various pentagonal tcp phases and the EDP is shown as an inset. Two things struck us immediately when we first obtained this EDP. First, how could these microdomains give a common diffraction pattern? This is very astonishing indeed if we look at Fig. 53 carefully. Quite a number of pentagonal tcp phases, such as C14 (L, L′, L″) and C15 (U, U′) Laves, μ, C and Zr_4Al_3(Z) phases, are present in such a small region and these domains are only a few nanometres in size. The structure of these microdomains must have a great deal in common. The pentagonal antiprisms, besides being parallel, may also have the same or similar orientation. Secondly, this EDP has a non-crystallographic five-fold symmetry. Moreover, the diffraction spots do not form a crossgrid corresponding to a two-dimensional section of a reciprical lattice as they usually do. In other words, no crystal lattice can be derived from this EDP. This seems rather unusual, but quite logical, if the minute size and many different structure types of these microdomains are taken into consideration. The translation order in these microdomains, though perfect, is only limited to a few nanometres and it is lost by averaging over so many differently oriented domains of different structure types. What is left is their common structural unit, the pentagonal antiprism, and this is the reason why the EDP shows a five-fold diffraction symmetry. Of course this will require all these pentagonal antiprisms not only being parallel but also having a similar orientation.

First, the structural models of various pentagonal tcp phases were carefully examined and it was found that not only differently oriented domains of a tcp phase, such as the two rotation domains of μ shown in Fig. 52, but also the various tcp phases, such as C14

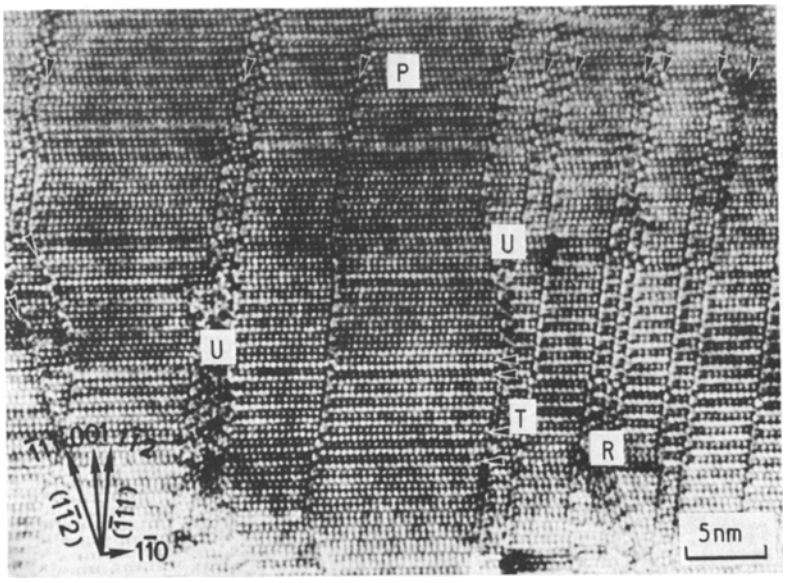

Figure 45 General mosaic appearance of the domain structure in μ. Arrows mark the domain boundaries on (0 0 1), ($\bar{1}$ 1 1) and (1 $\bar{1}$ 2). R indicates a rotation domain boundary.

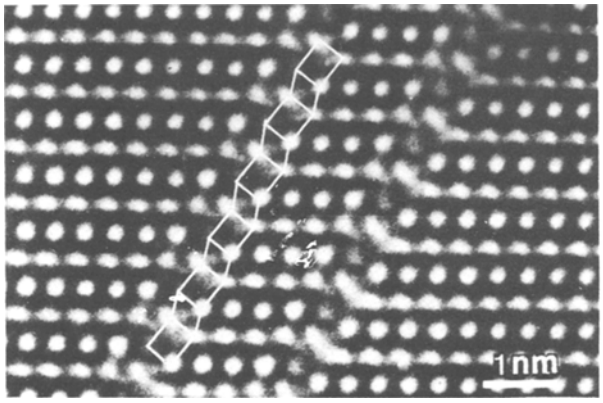

Figure 47 Structural image of two (1 $\bar{1}$ $\bar{1}$) domain boundaries in C14 Laves phase, one of which is outlined as a slab of μ.

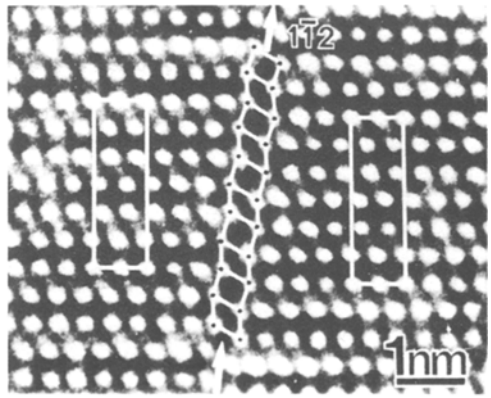

Figure 49 Structural image of ($\bar{1}$ 1 1) domain boundary in μ, in which a slab of C14 Laves phase is outlined.

Laves, μ, C and W_2FeSi in Fig. 48, all consist of similarly oriented pentagonal antiprisms. The only difference is a translation of $z/2$ in the direction of the five-fold axis when two pentagonal antiprisms are connected by face-sharing (i.e. with a separation of s). However, in the projection along this axis, even this difference is lost.

Secondly, all the EDPs of these pentagonal tcp phases have ten evenly distributed strong diffraction spots lying on the periphery of these EDPs (Figs. 17b and 33). If these EDPs are superimposed at the correct orientation, a composite EDP rather similar to that shown as the inset in Fig. 53 has been obtained. This not only explains the fact that the inset in Fig. 53 is the EDP of a great number of pentagonal microdomains, but also implies that it is the EDP or Fourier transform of many similarly oriented pentagonal antiprisms.

Finally, the Fourier transform of a single pentagonal antiprism is calculated and it corresponds precisely to the EDP in Fig. 53 [59]. The maxima occur in pairs with a five-fold symmetry, the former coming from two prisms in antisymmetrical positions and the latter from the pentagonal nature of these prisms. In other words, the pentagonal antiprism is the subunit or building block of the structure of various pentagonal tcp phases, therefore there must be a superunit in the reciprocal lattice showing this symmetry. The ten strong diffraction spots on the outermost ring of the EDPs are just a manifestation of this superunit.

The above discussion also applies to the tcp phases made up of hexagonal antiprisms. All these antiprisms have the same orientation and therefore a long-range orientation order also exists in σ (Fig. 1d), H (Fig. 19b), F (Fig. 24), K (Fig. 27), J (Fig. 30) and

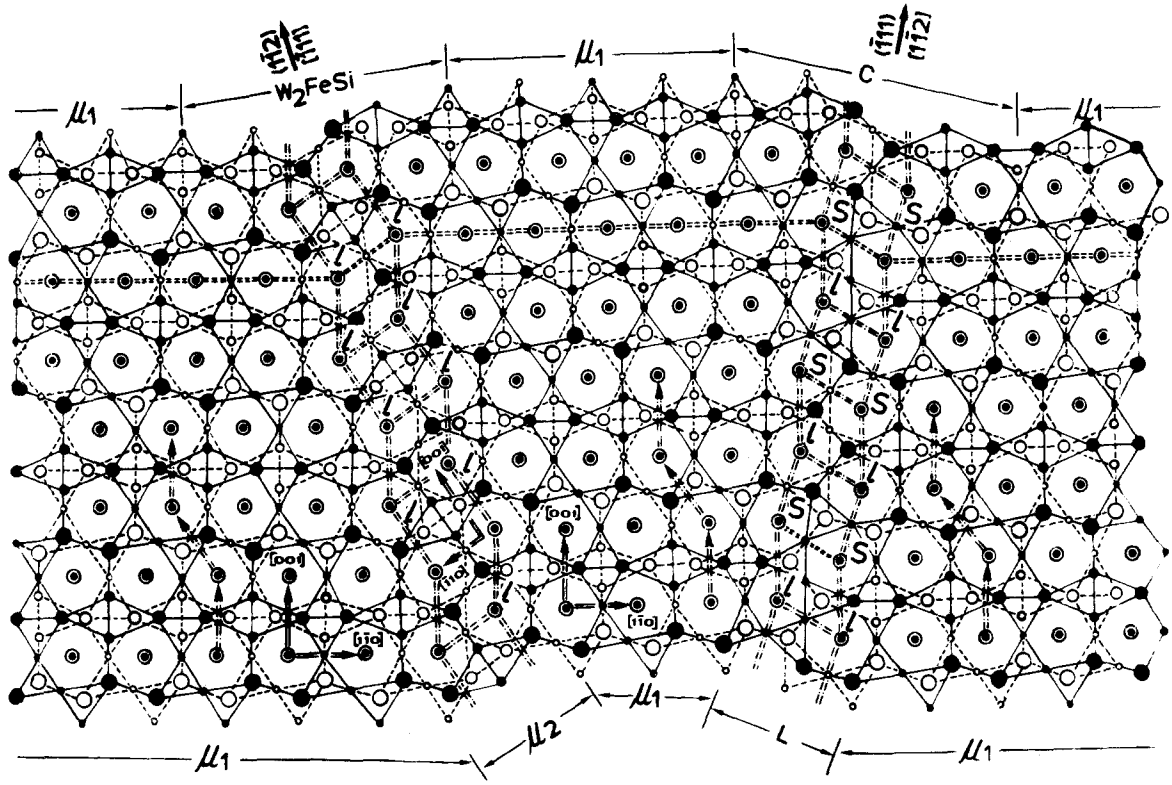

Figure 48 Structure model of translation domain boundaries on (1 $\bar{1}$ 2) and ($\bar{1}$ 1 1) of μ. On the left, the boundary is a differently oriented μ slab with *–l–l–l–l–* separations between pentagonal antiprisms. On the right, it is a C14 Laves or C slab with *–s–l–s–l–* separations.

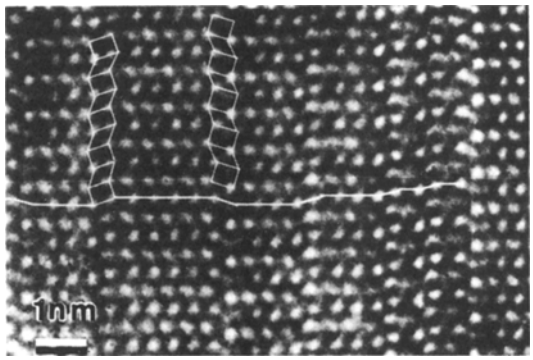

Figure 50 Structural image of a set of $(1\bar{1}0)$ domain boundaries in C14 Laves phase, in which two differently oriented Zr_4Al_3 units can be identified.

their translation as well as rotation domain boundaries (Figs. 37b, 38b, and 42b). In the reciprocal space there are twelve evenly distributed strong diffraction spots laying on the outermost ring of the EDPs.

In the above discussion, antiprisms of the same or similar orientation are arranged orderly within a range of a few nanometres. If the size of microdomain diminishes, this translation order will also diminish until it at last vanishes. In this case only the long-range orientation order remains and an EDP such as that in Fig. 53 will result. In a study of the phase in a

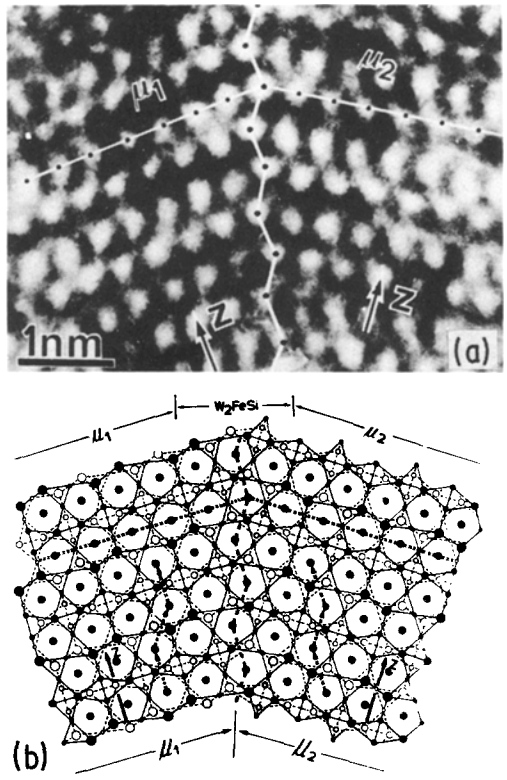

Figure 52 (a) Structural image of two rotation domains of μ, and (b) its structure model.

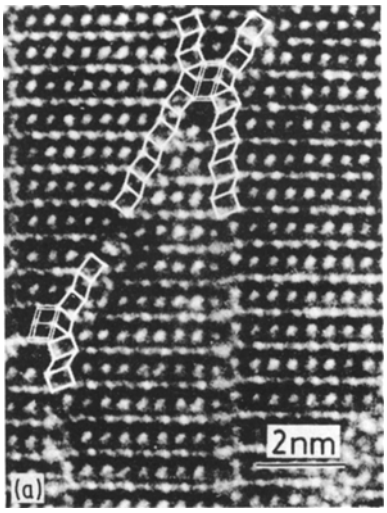

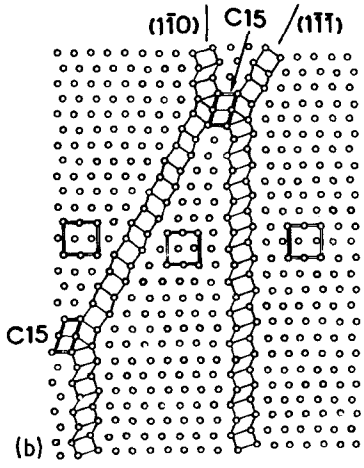

Figure 51 (a) [1 1 0] structural image, and (b) its schematic diagram of the intersection of $(1\bar{1}0)$ and $(1\bar{1}1)$ domain boundaries in C14 Laves phase. Three layers of ABC sequence (C15 Laves phase, $MgCu_2$ type) occur at the intersection

spun quenched Al–14 at % Mn alloy, Shechtman *et al.* [61] have recently obtained EDPs with sharp diffraction spots displaying $\bar{5}\bar{3}m$ icosahedral symmetry. Such EDPs have also been found in a spun quenched $(Ti, V)_2Ni$ alloy in our laboratory [60] and Fig. 54 shows one of them exhibiting the $\bar{5}$ symmetry. The similarity between the EDPs in Figs. 53 and 54 is quite obvious, implying the presence of long-range orientation order of pentagonal antiprisms or icosahedra. However, the spots in Fig. 54 are as sharp as those from a crystalline phase. Since five-fold translation symmetry is prohibited by classical crystallography, this was named a quasi-crystalline state. Experiments and theory [62] seem to indicate that there is a modified form of translation order similar to the case of filling a two-dimentional space with two kinds of "Penrose tiles" [63] displaying five-fold symmetry. Obviously, the quasi-crystalline state is both of theoretical as well as of practical importance and this will be an interesting field of research for material scientists.

7. Conclusions

1. The structures of various tcp phases, especially those consisting of pentagonal or hexagonal antiprisms, are built up from some elementary units and therefore they form a hierarchy of structures from simple to complex ones.

2. HREM can image each pentagonal or hexagonal antiprism as a bright disc or dot and therefore can reveal their arrangement in a plane perpendicular to these antiprisms. In other words, one can "read" the tessellation of these antiprisms directly from the high-resolution image. By this means, four new hexagonal

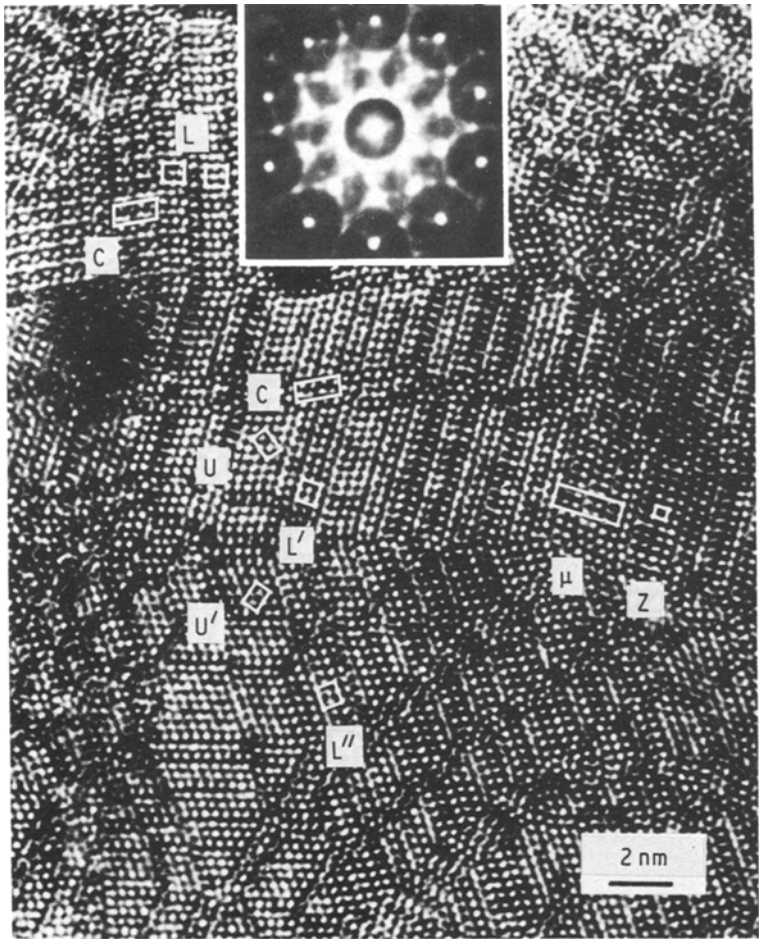

Figure 53 General mosaic appearance of a large number of microdomains of C14 Laves (L, L′ and L″), C15 Laves (U and U′), C and Zr_4Al_3 (Z) phases of only a few nanometres in size. Its five-fold diffraction pattern is shown as an inset.

σ-related tcp phases (H, F, K and J) and two new pentagonal tcp phases (C and C_1) have been found.

3. HREM can also reveal the local structure at the nanometer or even the atomic level. This is especially useful in the study of domain boundary structures in various tcp phases. The arrangement of antiprisms at the boundaries is not only in perfect order but also may have a configuration identical to another tcp phase or to a different orientation.

4. The antiprisms in different tcp phases or in different domains of a tcp phase all have the same or similar orientation and this makes it possible to determine the characteristics of these antiprisms from these EDPs. A hexagonal tcp phase will have twelve evenly distributed strong spots lying on the outermost ring of its EDP while a pentagonal phase will have only ten spots.

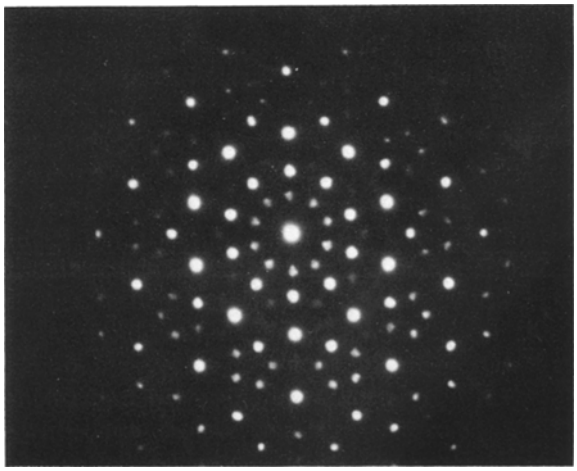

Figure 54 The five-fold diffraction pattern with sharp diffraction spots of the "icosahedral phase" found in a spun quenched $(Ti_{0.9}V_{0.1})_2Ni$ alloy.

Acknowledgement

This work is supported finanacially by a grant from the Science Fund of the Chinese Academy of Sciences (Academia Sinica), which is gratefully acknowledged.

References

1. F. C. BAIN and A. A. GRIFFITH, *Trans. AIME* **75** (1927) 166.
2. T. B. FRIAUF, *J. Amer. Chem. Soc.* **49** (1927) 3107.
3. F. LAVES and K. LÖHBERG, *Nachr. Gött. Akad. D. Wiss, Math. Phys. Kl. IV, Neue Folge* **1** (1934) 59.
4. H. ARNFELT and A. WESTGREN, *Jernkontor. Ann.* **119** (1935) 185.
5. D. P. SHOEMAKER and B. G. BERGMAN, *J. Amer. Chem. Soc.* **72** (1950) 5793.
6. S. RIDEOUT, W. D. MANLY, E. K. KAMEN, B. S. LEMENT and P. A. BECK, *Trans. TMS AIME* **191** (1951) 872.
7. D. P. SHOEMAKER, C. B. SHOEMAKER and F. C. WILSON, *Acta Crystallogr.* **10** (1957) 1.
8. Y. KOMURA, W. G. SLY and D. P. SHOEMAKER, *ibid.* **13** (1960) 575.
9. C. B. SHOEMAKER and D. P. SHOEMAKER, *ibid.* **16** (1963) 997.
10. *Idem, ibid.* **23** (1967) 231.
11. H. HARTMANN, F. FBERT and O. BRETSCHNEIDER, *Z. Anorg, Allg. Chem.* **198** (1931) 116.
12. C. G. WILSON, D. K. THOMAS and F. J. SPOONER, *Acta Crystallogr.* **13** (1960) 56.
13. F. C. FRANK and J. S. KASPER, *ibid.* **11** (1958) 184.
14. *Idem, ibid.* **12** (1959) 483.

15. C. B. SHOEMAKER and D. P. SHOEMAKER, in "Developments in the Structural Chemistry of Alloy Phases" (Plenum, New York, 1969) p. 107.
16. S. ANDERSSON, *J. Solid State Chem.* **23** (1978) 191.
17. M. J. MARCINKOWSKI and D. S. MILLER, *Phil. Mag.* **7** (1962) 1025.
18. K. YAGISAWA and H. FUJITA, *Jpn. J. Appl. Phys.* **6** (1967) 826.
19. C. W. ALLEN, D. DELAVIGNETTE and S. AMELINCKX, *Phys. Status Solidi (a)* **9** (1972) 237.
20. L. STENBERG and S. ANDERSSON, *J. Solid State Chem.* **28** (1979) 269.
21. M. HIRABAYASHI, *Trans. Jpn. Inst. Metals* **24** (1983) 315.
22. Y. KOMURA, S. TAKEDA and M. TAKATA, *ibid.* **24** (1983) 410.
23. T. ISHIMASA, Y. KITANO and Y. KOMURA, *J. Solid State Chem.* **36** (1980) 74.
24. *Idem, Phys. Status Solidi (a)* **66** (1981) 703.
25. Y. KITANO, Y. KOMURA, H. KAJIWARA and E. WATANABE, *Acta Crystallogr.* **A36** (1980) 16.
26. L. STENBERG, *Chem. Scripta* **14** (1978/79) 219.
27. D. X. LI, L. STENBERG and S. ANDERSSON, *J. Solid State Chem.* **48** (1983) 368.
28. *Idem,* unpublished work.
29. K. HIRAGA, T. YAMAMOTO and M. HIRABAYASHI, *Trans. Jpn. Inst. Metals* **24** (1983) 421.
30. J. S. KASPER, in "Theory of Alloy Phases" (American Society of Metals, Cleveland, 1956) p. 264.
31. W. B. PEARSON, in "The Crystal Chemistry and Physics of Metals and Alloys" (Wiley–Interscience, New York, 1972) p. 44.
32. A. K. SINHA, in "Topologically Close-Packed Structures of Transition Metal Alloys" (Pergamon Press, London, 1972) p. 1.
33. H. Q. YE, D. X. LI and K. H. KUO, *Acta Crystallogr.* **B40** (1984) 461.
34. H. Q. YE and K. H. KUO, *Phil. Mag.* **A50** (1984) 117.
35. D. X. LI and K. H. KUO, *Acta Crystallogr.* (1985) in press.
36. H. Q. YE, D. N. WANG and K. H. KUO, Proceedings of the 3rd Asia-Pacific Conference on Electron Microscopy, edited by Chung Mui Fatt (Applied Research Corporation, Singapore, 1984) p. 170.
37. D. I. BARDOS and P. A. BECK, *Trans. AIME* **236** (1966) 64.
38. P. I. KRIPYAKEVICH and Y. P. YARMOLYUK, *Dopl. Akad. Nauk. Ukr, SSR. Ser. A* **32** (1970) 948.
39. *Idem, ibid.* **36** (1974) 460.
40. C. B. SHOEMAKER, *Acta Crystallogr.* **B39** (1983) 654.
41. K. H. KUO, *JEOL News* **22E** (3) (1984) 11.
42. K. ISHIZUKA, *Acta Crystallogr.* **A38** (1982) 773.
43. J. M. COWLEY, in "Diffraction Physics" (North-Holland, Amsterdam, 1975) p. 275.
44. J. H. C. SPENCE, in "Experimental High-resolution Electron Microscopy" (Clarendon Press, Oxford, 1981) p. 121.
45. H. Q. YE, D. X. LI and K. H. KUO, *Phil. Mag.* **A51** (1985) 829.
46. H. Q. YE, Z. ZHANG and K. H. KUO, *Phys. Stat. Sol. (a)* **83** (1984) 77.
47. A. KLUG, *Chem. Scripta* **14** (1978/79) 245.
48. J. W. STEEDS, in "Introduction to Analytical Electron Microscopy", edited by J. J. Hren, J. I. Goldstein and D. C. Joy (Plenum, New York, 1979) p. 387.
49. Y. P. LIN and J. W. STEEDS, *Acta Crystallogr.* (1985) in press.
50. B. F. BUXTON, J. A. EADES, J. W. STEEDS and G. M. RACKHAM, *Phil. Trans. R. Soc.* **281** (1976) 171.
51. H. Q. YE, D. X. LI and K. H. KUO, Proceedings of the 3rd Asia-Pacific Conference on Electron Microscopy, edited by Chung Mui Fatt (Applied Research Corporation, (Singapore, 1984) p. 146.
52. D. N. WANG, H. Q. YE and K. H. KUO, *Acta Crystallogr.* (1985) in press.
53. K. H. KUO, H. Q. YE and D. X. LI, *J. Electron Microsc. Tech.* **3** (1986).
54. D. X. LI, H. Q. YE and K. H. KUO, *Phil. Mag.* **A50** (1984) 531.
55. H. Q. YE, D. X. LI and K. H. KUO, in "Electron Microscopy 1984" edited by A. Csanady, P. Röhlich and D. Szabo (Programme Committee of the Eighth European Congress on Electron Microscopy, Budapest, 1984) p. 213.
56. D. N. WANG, H. Q. YE and K. H. KUO, *ibid.* (1984) 809.
57. H. Q. YE, D. N. WANG and K. H. KUO, *Phil. Mag.* **A51** (1985) 839.
58. D. X. LI and K. H. KUO, *ibid.* **A51** (1985) 849.
59. H. Q. YE, D. N. WANG and K. H. KUO, *Ultramicroscopy* **16** (1985) 273.
60. Z. ZHANG, H. Q. YE and K. H. KUO, *Phil. Mag.* (1985) in press.
61. D. SHECHTMAN, I. BLECH, D. GRATIAS and J. W. CAHN, *Phys. Rev. Lett.* **53** (1984) 1951.
62. D. LEVINE and P. J. STEINHARDT, *ibid.* **53** (1984) 2477.
63. R. PENROSE, *Bull. Inst. Math. Appl.* **10** (1974) 266.

Received 9 July
and accepted 20 August 1985